# Additively manufactured IN718 in thin wall and narrow flow channel geometries: Effects of post-processing and wall thickness on tensile and fatigue behaviors

Nabeel Ahmad [a,b], Shuai Shao [a,b], Mohsen Seifi [c], Nima Shamsaei [a,b,*]

[a] National Center for Additive Manufacturing Excellence (NCAME), Auburn University, Auburn, AL 36849, USA
[b] Department of Mechanical Engineering, Auburn University, Auburn AL36849, USA
[c] ASTM International, Washington, DC 20036, USA

## ARTICLE INFO

## ABSTRACT

Using additively manufactured (AM) tubular IN718 specimens, this study was conducted to understand the effects of wall thickness, surface machining, and hot isostatic pressing (HIP) on tensile and fatigue behaviors. The tubular specimens with thin wall (TW) features and narrow flow channels (NFC) had machined external surfaces and a combination of different internal surface (machined vs. unmachined) and heat treatment (with HIP vs. without HIP) conditions. On one hand, in terms of tensile properties, HIP was found to decrease strength while slightly improving ductility under quasi-static loading. Both surface machining and larger wall thickness were found to improve ductility without influencing the strength. On the other hand, HIP, surface machining, and wall thickness had no measurable influence on fatigue performance in the low and mid cycle fatigue regimes. Some positive effects of wall thickness on fatigue life were noticed in the high cycle fatigue regime for TW specimens undergone HIP and internal surface machining. The results suggested that the post-processing steps of AM IN718 TW and NFC parts could potentially be eliminated to reduce production cost and lead time if the targeted applications were fatigue critical in low and mid cycle fatigue regimes.

## 1. Introduction

Thin wall (TW) and narrow flow channel (NFC) geometries are widely used in some components of aircraft, storage vessels, and heat exchangers. These geometries often have complex features and machining poses significant challenges (in some cases such geometries are not even machinable) as high stresses/temperatures during the cutting operation cause distortion and dimensional errors in produced parts [1]. This issue is exacerbated while cutting hard-to-machine alloys such as IN718 [2], which, due to its excellent corrosion resistance and elevated temperature mechanical properties, is often found in harsh environments [3]. Interestingly, IN718 possesses decent weldability (due to its low Ti and Mo content) making it compatible with additive

manufacturing (AM) processes, whose near-net shaping capability significantly minimizes the need for machining and thus reduces production costs [4,5]. Nevertheless, several issues including elemental segregation, volumetric defects, and surface roughness from the AM process can adversely affect the mechanical properties of the fabricated parts [6–8], which generally necessitates post-processing heat treatments (HT), hot isostatic pressing (HIP), and surface machining [9], respectively.

The HIP cycle was shown to homogenize the microstructure and reduce/eliminate volumetric defects in IN718 due to high temperatures (1100–1180 °C) and pressure (~100 MPa) [10,11]. Studies by Balachandramurthi et al. [12] and Sadeghi et al. [13] on laser powder bed fused (L-PBF) IN718 showed slightly better fatigue resistance of specimens underwent both HIP & HT in low cycle fatigue (LCF) and mid cycle

**Nomenclature**

| | |
|---|---|
| $\gamma$ | Matrix phase in IN718. |
| $\delta$ | Brittle phase in IN718. |
| $\varepsilon_a$ | Strain amplitude. |
| $\Delta\varepsilon_e/2$ | Elastic strain amplitude. |
| $\Delta\varepsilon_p/2$ | Plastic strain amplitude. |
| $\sigma_a$ | Stress amplitude. |
| $\sigma_m$ | Mean stress. |
| EL | Elongation to failure. |
| $2\,N_f$ | Reversals to failure. |
| $R_a$ | Arithmetic mean height. |
| $R_v$ | Maximum valley depth. |
| $R_\varepsilon$ | The ratio of minimum strain to maximum strain. |
| UTS | Ultimate tensile strength. |
| YS | Yield strength. |

fatigue (MCF) regimes compared to heat treated (HT) only specimens. This could primarily be attributed to the dissolution of the populous detrimental δ phases in the HIP & HT specimens. In contrast, Gribben et al. [14,15] revealed that HIP & HT condition was not beneficial to mechanical performance of L-PBF IN718. The high cycle fatigue (HCF) results indicated lower fatigue resistance of HIP & HT specimens compared to HT ones. They attributed this behavior to coarsened microstructure, and HIP induced annealing twins, which caused early crack initiations. Interestingly, a study by Muhammad et al. [16] on L-PBF IN718 in HT only condition showed crack initiations from facets due to the operation of persistent slip bands (PSBs), despite the presence of relatively large volumetric defects (>40 μm) in the specimens. Combining crystal plasticity simulations and experiments, Dodaran et al. [17] showed that PSB-mediated fatigue crack initiation life of IN718 was inversely related to the free slip distance within grains, and thus, the relatively large grain size in the HT only L-PBF IN718 favored PSB-mediated fatigue crack initiation. As such, the application of HIP can further coarsen the microstructure, and therefore, reduce the fatigue resistance. These recently demonstrated insensitivity of AM IN718 fatigue properties to volumetric defects can potentially challenge the present industrial practice of ubiquitous application of HIP.

Surface condition is another factor that can affect the mechanical properties of AM IN718 parts to varying degrees. For tensile properties, excessively high surface roughness (such as those typical of the electron powder bed fusion (E-PBF)) was shown by Zhao et al. [18] to significantly reduce elongation to failure (EL) by ~90% as compared to specimens with machined surfaces, and induce brittle fracture at stresses ~20% below yield strength (YS). On the other hand, moderate surface roughness (such as those typical of L-PBF processes), is expected to only slightly reduce EL and generally should not debit strength [19,20]. For fatigue properties, Lee et al. [21] showed that the L-PBF IN718 specimens with as-built surface roughness had significantly shorter fatigue lives in the HCF regime than the machined and drag-finished ones. In mid to low cycle fatigue (MCF to LCF) regimes, the impact was not notable. In some cases, surface machining (especially shallow machining often desirable for IN718 due to its poor machinability) may not be beneficial for AM IN718 parts at all, since it could expose large sub-surface volumetric defects which can be as detrimental as the surface roughness [18,22]. As such, depending on the design goal of the targeted applications (i.e., guarding against first cycle yielding, LCF finite life, or infinite life, etc.) machining as a necessary finishing step for IN718 may be debatable. Keeping this in view, a comprehensive study on the effect of surface machining on mechanical performance of L-PBF IN718 is needed. Knowledge gained from this study will contribute to "Surface finish" gap (P4) reported by America Makes & ANSI additive manufacturing standardization collaborative (AMSC) [23].

Tensile and fatigue data of AM parts are typically generated using specimens with standardized geometries and dimensions [16,21,24], that may be significantly different from those of the in-service components such as heat exchangers, which often have complex geometries of varying wall thicknesses. However, variation in geometry may result in different measured mechanical properties [25,26]. Accordingly, data generated in the laboratory settings may not be transferable for designing NFC and TW. For instance, Razavi et al. [27] reported that EL of E-PBF Ti-6Al-4 V flat tensile geometries with thickness of 5 mm were over three times as much as the one measured from specimens with a thickness of 1 mm. Despite its potential impact, there exist very limited studies on the effect of wall thickness on LCF, HCF, and quasi-static tensile behaviors, and the limited ones available mainly focus on L-PBF SS 316 L [28], and E-PBF Ti-6Al-4 V alloys [27].

The objective of this study was to investigate the effects of post-processing, including HIP and machining, and specimens wall thickness on the mechanical properties measured from two distinct specimen geometries – TW and NFC. The TW and NFC IN718 specimens with different wall thicknesses were fabricated using L-PBF. Post-fabrication, all specimens went through stress relief (SR), solution annealing (SA), and 2-step aging as well as external surface machining. HIP and internal surface machining were applied to selected specimens to isolate their effects on both tensile and fatigue behaviors. This article is organized as following: in Section 2, the experimental procedure is described. In Section 3, experimental results including microstructure analysis (Section 3.1), surface roughness (Section 3.2), tensile (Section 3.3), and fatigue properties (Section 3.4) are presented. Results are discussed in Section 4, and finally, major conclusions are listed in Section 5.

## 2. Experimental procedures

### 2.1. Specimen design and fabrication

The drawings of different geometries (machined to the final dimensions) are exhibited in Fig. 1(a) and Fig. 1(c). These geometries were separated into two groups: TW and NFC. TW geometries were designed according to ASTM E2207 [29]. Since there were no standardized geometries available for NFC specimens, concepts of TW geometries were adopted to design the NFC ones. TW group of geometries maintained the same outer diameter (OD), while thickness (t) was sequentially increased from 0.50 to 1.25 mm. Similar to the TW specimens, OD of NFC geometries was maintained the same, while thickness was increased from 1 to 2.5 mm. Note that the OD at the grip and gage sections was oversized by 2 mm for all specimens, and the inner diameter (ID) was undersized by 1 mm for all the ID machined specimens to allow adequate surface machining (1 and 0.50 mm depths for OD and ID machining, respectively).

The build layouts of TW and NFC specimens are exhibited in Fig. 1(b) & (d), respectively. The specimens are color-coded in Fig. 1(b) & (d) according to the specimens' wall thickness and ID. For TW specimens (see Fig. 1(b)), red, blue, and gray colors correspond to 1.25, 0.75, and 0.50 mm wall thicknesses, respectively. For NFC specimens (see Fig. 1(d)), green and blue colors correspond to the specimens with the wall thicknesses of 1 and 2.5 mm, respectively. As seen in the build layouts, the specimens of each geometry were evenly distributed throughout the build platform to minimize location dependency of measured mechanical properties. In addition, for fatigue tests at each stress/strain level, specimens were intentionally chosen from different locations.

The pre-alloyed argon gas-atomized IN718 powder, supplied by Carpenter Additive, was used in the virgin state to fabricate specimens using an EOS M290 machine – an L-PBF platform. The EOS recommended process parameters, listed in Table 1, were employed for fabrication.
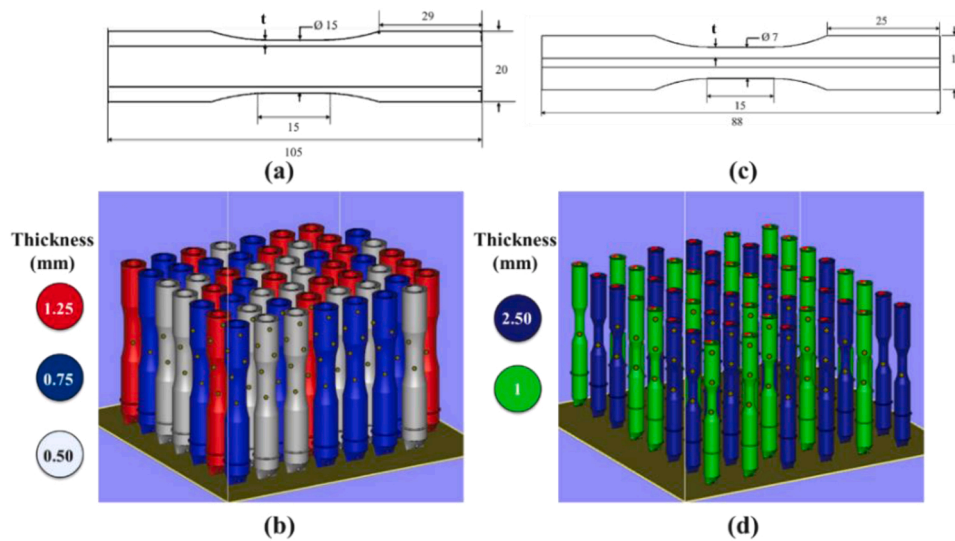
**Fig. 1.** Drawings and build layouts of TW and NFC specimens: (a)-(b) dimensions and the build layout of TW specimens; (c)-(d) dimensions and build layout of NFC specimens. Although TW and NFC groups of geometries maintained the same OD and gage length, the thickness was varied. Different colors in the build layouts indicate the thickness of specimens. All dimensions are in mm.

**Table 1**

Core process parameters used for fabrication of L-PBF IN718.

| | |
|---|---|
| **Power (W)** | 285 |
| **Speed (mm/s)** | 960 |
| **Hatching Distance (mm)** | 0.11 |
| **Stripe Width (mm)** | 10 |
| **Layer Thickness (mm)** | 0.04 |
| **Layer Rotation Angle** | 67° |
| **Hatch Pattern** | Stripe |

### 2.2. HT procedures and post-processing conditions

Regardless of the geometry and surface condition, SR was performed according to ASTM F3301 [30] in a high temperature box furnace, while SA and 2-step aging were carried out on all the NFC and TW geometries following AMS 2774 F [31] in a vacuum furnace with argon quench capability as shown in Table 2. Baseline properties were obtained from NFC and TW specimens that were HIP and machined from both internal and external surfaces (referred to as HIP + Machined). Based on this, the mechanical performance debits associated with avoiding HIP and/or internal surface machining, if any, were determined with the NonHIP + Unmachined and HIP + Unmachined specimens. The ID and OD of specimens were machined on a lathe using reamer and turning tools, respectively. OD surfaces of all specimens were machined and polished, while the ID surfaces of specimens were only machined. Detailed specimens' conditions along with their designations are listed in Table 3.

**Table 2**

HT schedule used for this study.

| Condition | SR | HIP | SA | 2-Step Aging |
|---|---|---|---|---|
| HIP + HT | 925 °C/ 1 hr | 1120 °C/4 hrs at 100 MPa | 960 °C/ 1 hr | 720 °C/8 hrs, cool to 620 °C/10 hrs |
| NonHIP + HT | 925 °C/ 1 hr | – | 960 °C/ 1 hr | 720 °C for 8 hrs, cool to 620 °C /10 hrs |

**Table 3**

Mechanical testing plan followed for this study. Note that 3 tests per strain amplitude were performed at $\geq 0.003$ mm/mm and only 2 were conducted at 0.002 mm/mm strain amplitude. "No. Wall Thicknesses" column represents the number of wall thicknesses for each post-processing condition.

| | Condition | No. Wall Thicknesses | No. Strain Amplitudes | No. Fatigue Tests | No. Tensile Tests |
|---|---|---|---|---|---|
| **TW** | HIP + Machined (H + M) | 3 | 4 | 33 | 6 |
| | NonHIP + Unmachined (NH + UM) | 3 | 4 | 33 | 6 |
| | HIP + Unmachined (H + UM) | 3 | 4 | 33 | 6 |
| **NFC** | HIP + Machined (H + M) | 2 | 4 | 22 | 4 |
| | NonHIP + Unmachined (NH + UM) | 2 | 4 | 22 | 4 |
| | HIP + Unmachined (H + UM) | 2 | 4 | 22 | 4 |

### 2.3. Microstructure analysis and fractography

Microstructural samples were excised from the gage section of specimens perpendicular to the build direction (radial plane), mounted on the epoxy, ground, and polished according to ASTM E3 [32]. Using a Zeiss Crossbeam 550 scanning electron microscope (SEM), back-scattered electron (BSE) imaging and electron backscatter diffraction (EBSD) analysis were conducted. EBSD scans were performed utilizing source voltage of 20 kV and a step size of ~2 μm. EBSD data were then post-processed using AzTec Crystal software by Oxford Instruments. With the EBSD data, the grain counts through the wall thickness of each TW geometry were measured with 5 repetitions. To analyze the fracture mechanisms, fracture surfaces were first cut using

an abrasive cutter under a coolant jet, cleaned using a sonicator to eradicate dust and dirt, then washed with distilled water and iso-propanol. Zeiss Crossbeam 550 SEM was used to examine the fracture surfaces of both tensile and fatigue specimens.

## 2.4. Surface roughness

Internal surface roughness was measured destructively by excising small coupons from test specimens longitudinally (i.e., parallel to build direction) from both machined and unmachined surfaces. These coupons were mounted and polished using reducing grit sizes and a Keyence optical microscope was used to obtain surface profiles. Surface profile lines of each condition was then extracted from the micrographs using an in-house MATLAB code. Surface roughness parameters such as arithmetic mean height ($R_a$) and maximum valley depth ($R_v$) were evaluated following ISO 4287 [33]. Surface roughness statistics for each condition was obtained from three profile lines.

## 2.5. Mechanical testing

Strain/displacement-controlled tensile tests were performed based on ASTM E8 [33] using an MTS servohydraulic machine with a 100 kN load capacity. A constant nominal strain rate of 0.001 mm/mm/s was maintained in all tests. In each test, an extensometer was held on the specimens up to the strain of 0.035 mm/mm followed by its detachment and the continuation of the test under displacement control until fracture. A total of 30 tensile tests (2 tests per condition) were performed and the 0.2% offset method was used to calculate the YS.

Uniaxial fully-reversed ($R_\varepsilon = \varepsilon_{min}/\varepsilon_{max} = -1$) strain-controlled fatigue tests were performed based on ASTM E606 [34] using an MTS servohydraulic machine with a 100 kN load capacity. An MTS mechanical extensometer was used to measure the strains at the gage section. Fatigue tests were conducted at strain amplitudes of 0.002 mm/mm (frequency ($f$) = 2.5 Hz), 0.003 mm/mm ($f$ = 1.67 Hz), 0.005 mm/mm ($f$ = 1 Hz), and 0.010 mm/mm ($f$ = 0.5 Hz). Note that $f$ was adjusted for each test based on the applied strain level to maintain a similar average cyclic strain rate of 0.020 mm/mm/s. Since the overall cyclic deformation was fully elastic at 0.003 mm/mm strain amplitude, fatigue tests at/below this strain level were switched to force-controlled mode after reaching ~2000 cycles; however, the extensometer was held on the specimens to record the strains during cyclic loading.

The detailed mechanical testing plan followed for this study, including designation convention for each condition, the number of fatigue and tensile tests per condition is listed in Table 3. A condition was designated according to the HT and surface condition of the internal surface. For example, NonHIP + Unmachined signifies the specimens that did not undergo HIP and possessed as-built internal surface. Each post-processing condition is abbreviated using initials which are used to describe different conditions from hereon. For example, NH + UM is short hand for NonHIP + Unmachined. As discussed before, all the specimens were HT (SR, SA, and 2-step aging) regardless of geometry or surface condition. Besides, the OD of all specimens was machined and polished. A total of 165 fatigue tests (99 on TW specimens, 66 on NFC ones) and 30 tensile tests were performed.

## 2.6. X-ray computed tomography (XCT)

High resolution XCT scans were performed on some specimens which were separately loaded at the 0.010 mm/mm strain amplitude for 25%

or 50% of the average expected fatigue life to examine the presence of fatigue cracks. Constrained by geometry, such scans were performed only on the regions near the internal surface of the NFC specimens at the gage sections. XCT was performed using Zeiss Xradia 620 Versa machine at the voxel size of 3 μm. A source voltage and power of 160 kV and 25 W were used, respectively. Volumetric reconstruction was performed using a Zeiss proprietary software with smooth Gaussian reconstruction filter. Reconstructed data was imported into ImageJ software for further processing. Three-dimensional fatigue crack rendering was performed using the ORS Dragonfly image processing software.

## 3. Experimental results

### 3.1. Microstructure analysis

Inverse pole figure (IPF) maps and BSE images obtained from the microstructural samples excised from the radial planes of TW t = 0.75 mm specimens in the HIP + HT and NonHIP + HT conditions are presented in Fig. 2. Since all specimens were HT, the two afore-mentioned conditions were referred to as simply HIP and NonHIP. As evident from the BSE micrographs, acicular δ phase and carbides were precipitated both along the grain boundaries and within grains in both HT conditions. The NonHIP sample (see Fig. 2(b) & (c)), however, had significantly higher volume fraction of δ phase compared to HIP one. Moreover, the as-solidified dendritic microstructure was evident in the NonHIP sample (see Fig. 2(b) & (c)), which was not the case for the HIP one (see Fig. 2(e) & (f)). Azadian et al. [35] showed that the precipitation of the δ phase should peak at approximately 900 °C, which implied that the δ phase may have been precipitated during/after the SR step. Following SA at 960 °C, which was below δ solvus SA temperature [3], δ phase persisted and precipitated in large fraction in the microstructure. Moreover, SA duration and temperature were not sufficient to completely eradicate dendritic microstructure resulting from rapid solidification. By contrast, the HIP step following SR was expected to dissolve δ phase completely as its prescribed thermal exposure of 4 hrs at temperature 1120 °C was significantly higher than the δ solvus between 1005 and 1015 °C [21]. The small volume fraction of δ phase visible in Fig. 2(e) & (f) could have been the result of SA, which was sub-δ solvus at 960 °C for only one hour, performed after HIP and SR.

The IPF maps indicated considerable grain growth in the HIP condition (see corresponding histograms in Fig. 2(g) & (h)). EBSD results showed that the equivalent circle diameter of grains of NonHIP and HIP samples were 18 ± 12 and 74 ± 80 μm, respectively. In addition, the HIP microstructure had numerous annealing twins, which were absent in the NonHIP samples (see Fig. 2(a)). Note that annealing twins were excluded while calculating grain sizes. The larger grain size of HIP samples was attributed to the relatively high HIP temperature and duration that favored grain growth and the dissolution of δ phase as grain boundary pinners.

Grain count through the wall thickness of each TW geometries is presented in Fig. 2(i). As expected, grain counts increased with an increase in thickness for both HIP and NonHIP conditions. The number of grains through the wall thickness of HIP specimens, however, were lower than NonHIP ones as HIP specimens possessed coarser grains. In addition, Fig. 2(j) showed similar number of grains per mm in HIP condition, whereas NonHIP samples showed gradual drop at larger thicknesses. This is ascribed to presence of finer grains close to the surface. The trend of grain counts across the thicknesses of NFC specimens were similar, therefore, the related plot is not included here.
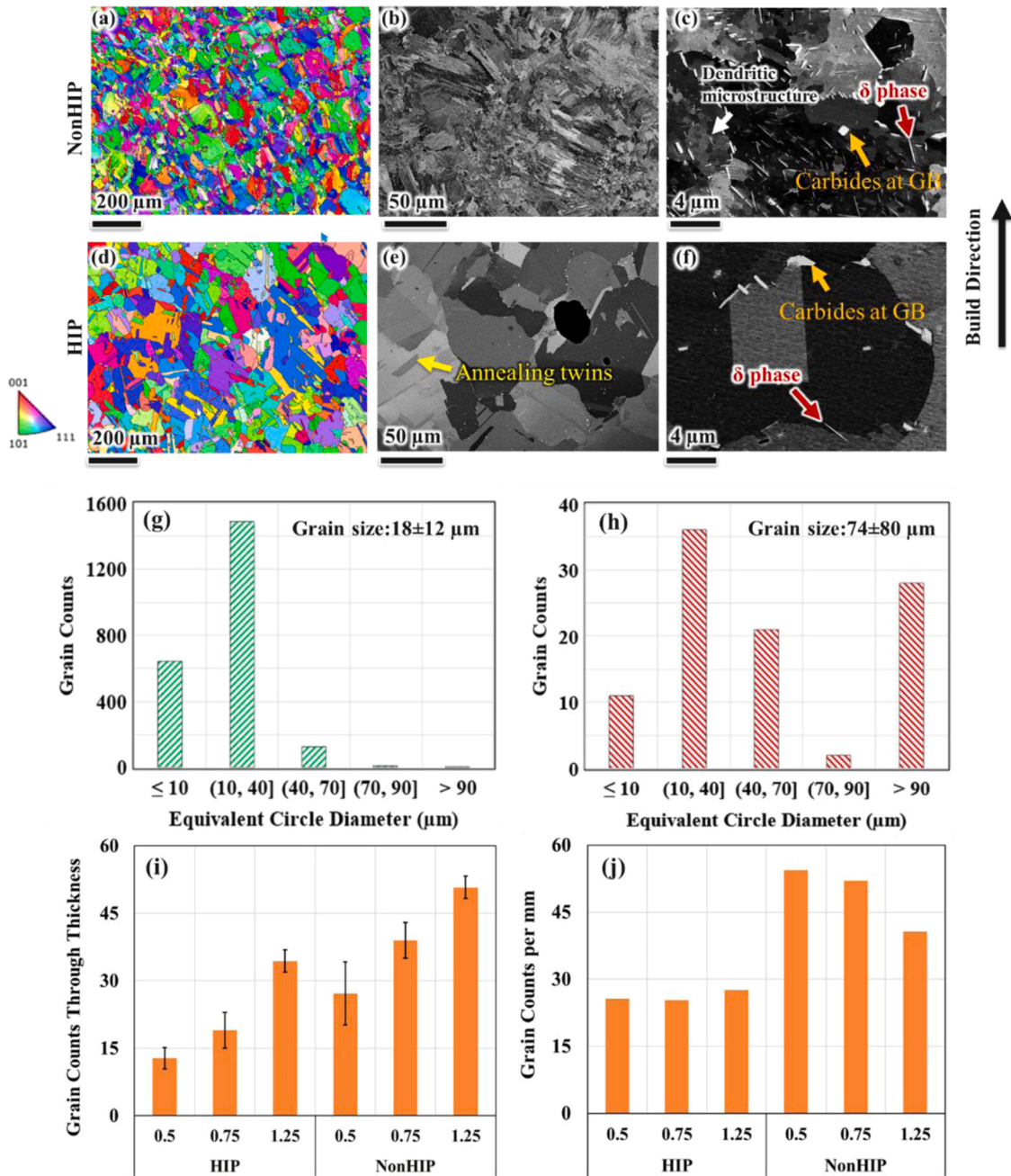
**Fig. 2.** IPF maps obtained from (a)-(c) NonHIP and (d)-(f) HIP samples. Charts in (g) and (h) show grain size histograms corresponding to (a) and (d), respectively. (i) and (j) exhibit grain counts through the wall thickness and grain counts per mm of TW geometries, respectively.

### 3.2. Surface roughness

Internal surface roughness was measured destructively by excising small coupons from test specimens longitudinally (i.e., parallel to build direction) from both machined and unmachined surfaces. Machined specimens, in general, possessed better internal surface finish compared to unmachined ones. However, there was an exception: NFC machined specimens with t = 2.5 mm had a large scatter in both $R_a$ and $R_v$ values which were covering the ranges of the unmachined ones. Poor surface quality of machined NFC specimens with t = 2.5 mm was due to deep machining grooves after reaming operation (see Section 4.3 for more discussion). Note that the OD surface roughness values of all TW and NFC specimens, presented with the dashed lines, were similar ($R_a \leq$ 0.5 μm, $R_v \leq 3$ μm) due to the identically applied machining and polishing process. Fig. 3.

### 3.3. Tensile results of TW and NFC specimens

An average and standard deviation of tensile properties including YS, ultimate tensile strength (UTS), and EL are presented in Table 4. In addition, to understand the effects of post-processing and specimen wall thickness, comparative bar plots are shown in Figs. 4 and 5. Since tensile results of both TW and NFC specimens showed little to no scatter, only two tests per condition/geometry were performed, and the error bars on each plot indicated the maximum-to-minimum ranges of tensile properties. Note that for calculating the stresses, while the measured diameter values were used, no corrections for surface roughness were made.

The effects of HT and surface condition on tensile properties for TW specimens are shown by the bar plots in Fig. 4(a), (b), & (c). As shown, machining the ID, regardless of specimen thickness, resulted in higher EL (compare H + M and H + UM conditions). This is expected as the
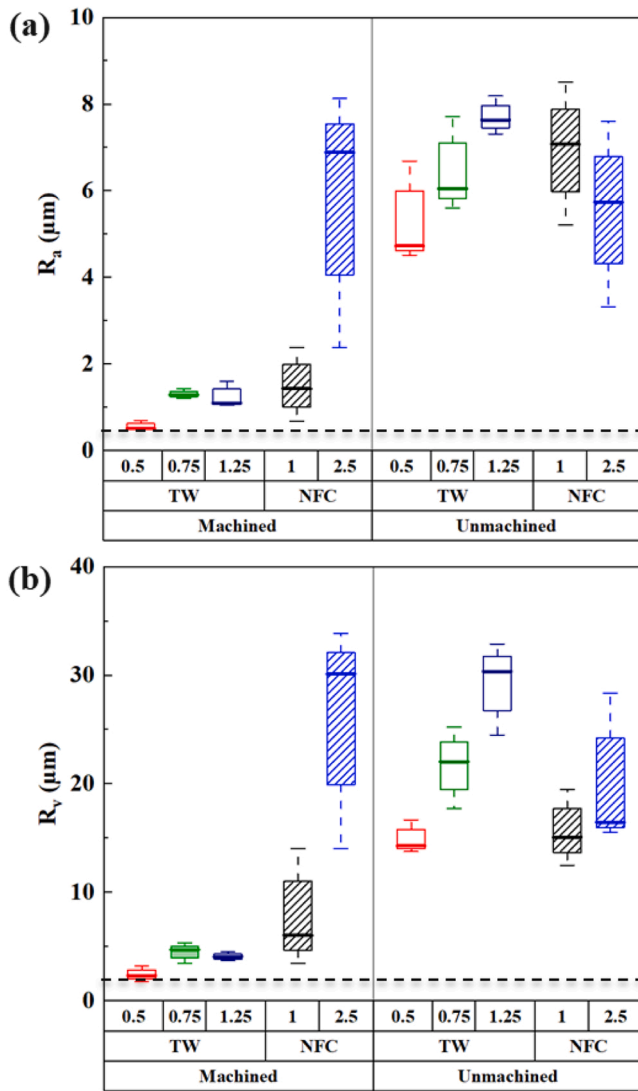
**Fig. 3.** A summary of ID roughness of both NFC and TW geometries in different surface conditions. Dashed lines in (a) and (b) indicate upper limits of OD roughness values. Abscissa represents thicknesses of TW and NFC geometries under machined and unmachined condition.

**Table 4**
Tensile properties of L-PBF IN718 TW and NFC specimens.

| Conditions | UTS (MPa) | YS (MPa) | %EL |
|---|---|---|---|
| H + M (TW t = 0.50 mm) | 1322 ± 6 | 1046 ± 2 | 21 ± 1 |
| H + UM (TW t = 0.50 mm) | 1325 ± 40 | 1044 ± 44 | 17 ± 0 |
| NH + UM (TW t = 0.50 mm) | 1442 ± 7 | 1165 ± 7 | 17 ± 0 |
| H + M (TW t = 0.75 mm) | 1265 ± 9 | 988 ± 8 | 24 ± 0 |
| H + UM (TW t = 0.75 mm) | 1295 ± 18 | 1004 ± 8 | 18 ± 0 |
| NH + UM (TW t = 0.75 mm) | 1373 ± 3 | 1110 ± 8 | 15 ± 1 |
| H + M (TW t = 1.25 mm) | 1351 ± 4 | 1074 ± 5 | 29 ± 0 |
| H + UM (TW t = 1.25 mm) | 1362 ± 7 | 1079 ± 1 | 19 ± 1 |
| NH + UM (TW t = 1.25 mm) | 1362 ± 5 | 1119 ± 6 | 18 ± 1 |
| H + M (NFC t = 2.5 mm) | 1355 ± 3 | 1082 ± 10 | 41 ± 1 |
| H + UM (NFC t = 2.5 mm) | 1348 ± 6 | 1053 ± 4 | 34 ± 1 |
| NH + UM (NFC t = 2.5 mm) | 1340 ± 3 | 1098 ± 23 | 27 ± 1 |
| H + M (NFC t = 1 mm) | 1348 ± 5 | 1036 ± 6 | 38 ± 1 |
| H + UM (NFC t = 1 mm) | 1327 ± 12 | 1046 ± 15 | 35 ± 2 |
| NH + UM (NFC t = 1 mm) | 1342 ± 4 | 1096 ± 10 | 28 ± 2 |

A replot of the tensile results highlighting the effects of wall thickness for different geometries and post-processing conditions is shown in Fig. 5. Note that observation on the effect of wall thickness on tensile behavior was made when other influencing factors (i.e., microstructure, and surface condition) were controlled. In the case of TW geometries (Fig. 5(a), (b), & (c)), EL increased with the increase in thickness in H +M condition. Although not as significant, there was also a similar effect of thickness on the EL in the H + UM condition as well. Note that there was no effect of thickness on EL in NH + UM specimens. NFC specimens (see Fig. 5(d)-(f)) showed a similar trend where EL increased with the increase in thickness for H + M condition (see Fig. 5(d)), slightly higher EL at larger thicknesses was noticed in H + UM specimens (see Fig. 5 (e)), and no effect of thickness on EL in NH + UM NFC specimens.

### 3.4. Fatigue results of TW and NFC specimens

Fatigue results with details such as surface/HIP conditions, build number, strain amplitude ($\varepsilon_a$), elastic ($\Delta\varepsilon_e/2$) and plastic strain ($\Delta\varepsilon_p/2$) amplitudes, mean stress ($\sigma_m$), stress amplitude ($\sigma_a$), and reversals to failure (2 $N_f$) for TW and NFC specimens at different wall thicknesses are tabulated in Tables 5 through 9. Note that the calculated mean stresses of the reported dataset were less than 10% of respective stress amplitudes; therefore, the effect of mean stress on the fatigue lives should not be significant. Stresses for each test was calculated using load reading and nominal cross-sectional area of specimen and error (if any) in measurements of gage diameter due to surface roughness was not corrected.

The tabulated strain-life fatigue data is visualized and presented in Fig. 6 separately for TW and NFC specimens. A factor of 3–4 scatter in the fatigue lives can be observed at 0.010, 0.005, and 0.003 mm/mm strain amplitudes across conditions for specimens of both geometries. Note that fatigue lives at $\varepsilon_a$ = 0.010 and 0.005 mm/mm at all conditions were within the LCF regime ($\sim 2 \times 10^4$ reversals to failure), while at $\varepsilon_a$ = 0.003 mm/mm and 0.002 mm/mm, they were MCF ($\sim 2 \times 10^5$ reversals to failure) and HCF ($> 2 \times 10^5$ reversals to failure) regimes, respectively. The total variation in fatigue lives due to different wall thicknesses and post-processing conditions was higher at $\varepsilon_a$ = 0.002 mm/mm (by over an order of magnitude). In general, the effect of the HIP on the TW and NFC specimens was not significant at $\varepsilon_a$ ≥ 0.003 mm/mm, regardless of the wall thickness and surface condition.

rough surface features essentially act as micro-notches, which could induce early onset of fracture. Higher EL of fully machined specimens was more pronounced for geometry with a thickness of 1.25 mm (Fig. 4 (c)). Moreover, NonHIP specimens, in general, showed slightly higher YS compared to HIP ones with the presence of the unmachined surface.

A summary of tensile results at different conditions for NFC specimens is presented in Fig. 4(d) & (e). The effects of surface condition and HIP on the tensile properties of NFC specimens were similar to the TW specimens. Regardless of geometry, fully machined specimens exhibited better EL compared to the specimens with unmachined ID, although the effect of machining on EL was less pronounced than the TW specimens. Moreover, NonHIP NFC specimens showed slightly higher YS; however, there was a reduction in EL compared to HIP specimens.

**Fig. 4.** Effects of surface condition and HIP on tensile properties for L-PBF IN718 TW and NFC specimens at different thicknesses: (a)-(c) TW specimens (d)-(e) NFC specimens. (f) The schematic of error bars shown on the bar charts indicating maximum, minimum, and mean values.
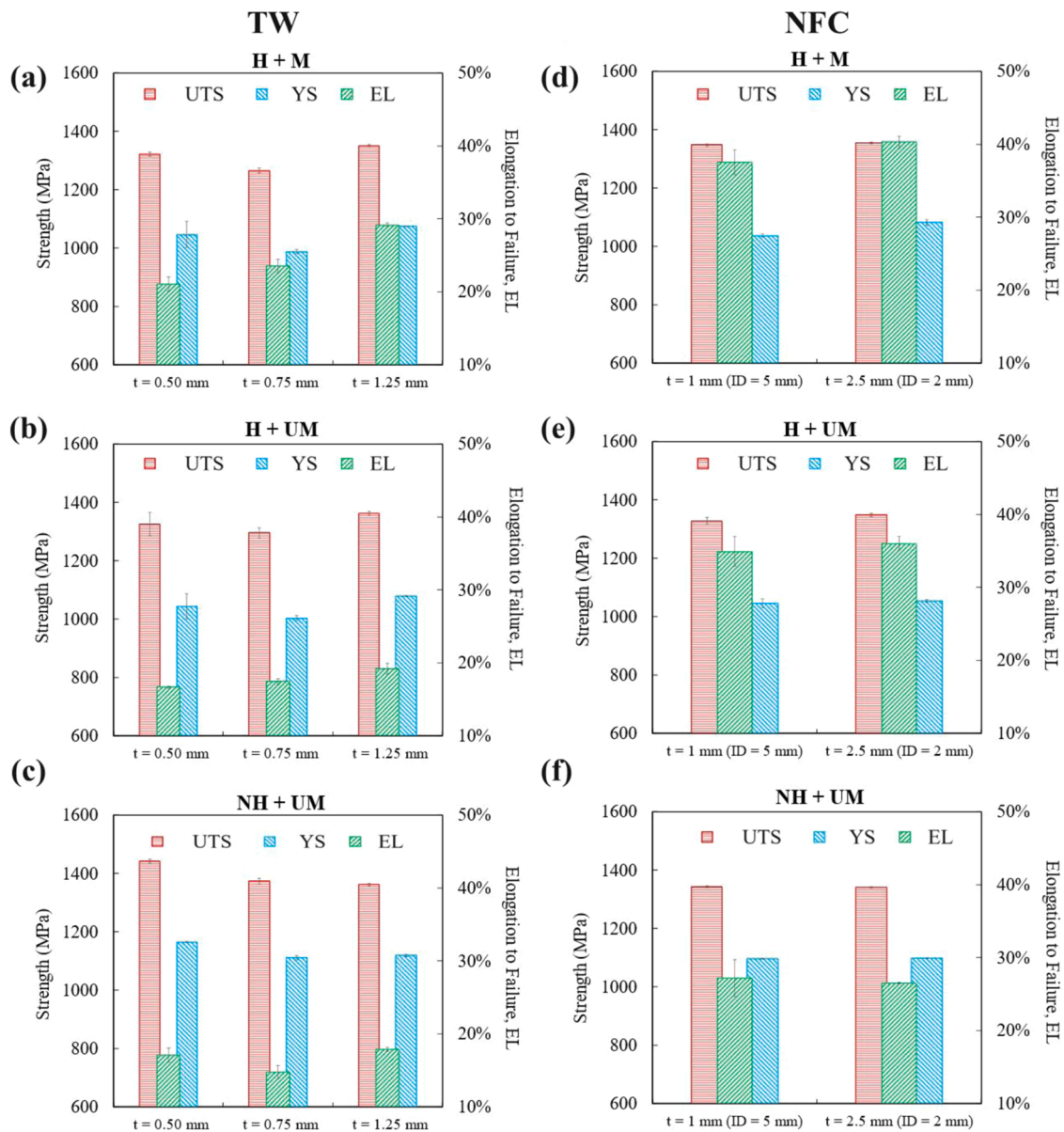
**Fig. 5.** Effect of specimen's wall thickness on tensile properties for L-PBF IN718 TW and NFC specimens at different post-processing conditions: (a)-(c) TW specimens (d)-(f) NFC specimens.

**Table 5**
Uniaxial, fully-reversed fatigue test results for L-PBF IN718 TW specimen with t = 0.50 mm.

| | Spec. ID | $\varepsilon_a$ (mm/mm) | $\Delta\varepsilon_e/2$ (mm/mm) | $\Delta\varepsilon_p/2$ (mm/mm) | $\sigma_a$ (MPa) | $\sigma_m$ (MPa) | $2 N_f$ |
|---|---|---|---|---|---|---|---|
| H + M | 1A4–3 | 0.002 | 0.002 | 0.000 | 377 | -1 | 419,178 |
| | 1A5–3 | 0.002 | 0.002 | 0.000 | 369 | 23 | 569,232 |
| | 1A6–1 | 0.003 | 0.003 | 0.000 | 592 | 0 | 68,266 |
| | 1A2–2 | 0.003 | 0.003 | 0.000 | 594 | 3 | 89,594 |
| | 1A5–2 | 0.003 | 0.003 | 0.000 | 555 | 18 | 76,344 |
| | 1A1–2 | 0.005 | 0.005 | 0.000 | 884 | -1 | 8796 |
| | 1A3–2 | 0.005 | 0.005 | 0.000 | 868 | 10 | 7194 |
| | 1A2–4 | 0.005 | 0.005 | 0.000 | 851 | 10 | 5528 |
| | 1A2–1 | 0.010 | 0.005 | 0.005 | 1012 | -24 | 770 |
| | 1A5–1 | 0.010 | 0.005 | 0.005 | 1003 | -4 | 1006 |
| | 1A6–2 | 0.010 | 0.006 | 0.004 | 993 | -18 | 660 |
| H + UM | 3A2–3 | 0.002 | 0.002 | 0.000 | 382 | 13 | 339,246 |
| | 3A3–3 | 0.002 | 0.002 | 0.000 | 379 | 13 | 307,360 |
| | 3A5–2 | 0.003 | 0.003 | 0.000 | 581 | -3 | 88,094 |
| | 3A6–2 | 0.003 | 0.003 | 0.000 | 579 | 11 | 102,560 |
| | 3A1–3 | 0.003 | 0.003 | 0.000 | 578 | 27 | 66,188 |
| | 3A1–2 | 0.005 | 0.004 | 0.001 | 850 | 31 | 7194 |
| | 3A2–2 | 0.005 | 0.005 | 0.000 | 891 | 38 | 6120 |
| | 3A3–3 | 0.005 | 0.005 | 0.000 | 867 | 72 | 6884 |
| | 3A4–1 | 0.010 | 0.005 | 0.005 | 947 | -23 | 1070 |
| | 3A5–1 | 0.010 | 0.005 | 0.005 | 973 | 55 | 1200 |
| | 3A4–2 | 0.010 | 0.005 | 0.005 | 971 | -16 | 932 |
| NH + UM | 2A4–4 | 0.002 | 0.002 | 0.000 | 339 | -9 | 1,090,292 |
| | 2A2–4 | 0.002 | 0.002 | 0.000 | 343 | -9 | 1,046,396 |
| | 2A1–2 | 0.003 | 0.003 | 0.000 | 526 | -2 | 176,906 |
| | 2A2–2 | 0.003 | 0.003 | 0.000 | 535 | -7 | 130,510 |
| | 2A3–3 | 0.003 | 0.003 | 0.000 | 538 | -9 | 120,118 |
| | 2A3–2 | 0.005 | 0.005 | 0.000 | 825 | -4 | 13,960 |
| | 2A4–2 | 0.005 | 0.005 | 0.000 | 820 | -17 | 14,232 |
| | 2A2–3 | 0.005 | 0.005 | 0.000 | 846 | 11 | 13,370 |
| | 2A5–2 | 0.010 | 0.006 | 0.004 | 999 | -3 | 912 |
| | 2A1–3 | 0.010 | 0.006 | 0.004 | 1039 | 4 | 1130 |
| | 2A6–2 | 0.010 | 0.006 | 0.004 | 1008 | -11 | 1152 |

**Table 6**
Uniaxial, fully-reversed fatigue test results for L-PBF IN718 TW specimens with t = 0.75 mm.

| | Spec. ID | $\varepsilon_a$ (mm/mm) | $\Delta\varepsilon_e/2$ (mm/mm) | $\Delta\varepsilon_p/2$ (mm/mm) | $\sigma_a$ (MPa) | $\sigma_m$ (MPa) | $2 N_f$ |
|---|---|---|---|---|---|---|---|
| H + M | 1B2–3 | 0.002 | 0.002 | 0.000 | 380 | 16 | 1,614,654 |
| | 1B2–4 | 0.002 | 0.002 | 0.000 | 387 | 13 | 1,211,400 |
| | 1B4–1 | 0.003 | 0.003 | 0.000 | 593 | -5 | 107,612 |
| | 1B2–2 | 0.003 | 0.003 | 0.000 | 605 | -1 | 91,552 |
| | 1B6–1 | 0.003 | 0.003 | 0.000 | 588 | 3 | 98,990 |
| | 1B1–1 | 0.005 | 0.004 | 0.001 | 830 | -3 | 12,520 |
| | 1B2–1 | 0.005 | 0.004 | 0.001 | 830 | -33 | 15,956 |
| | 1B5–2 | 0.005 | 0.005 | 0.001 | 838 | -21 | 8770 |
| | 1B1–2 | 0.010 | 0.005 | 0.005 | 988 | -22 | 1798 |
| | 1B3–2 | 0.010 | 0.005 | 0.005 | 990 | -27 | 1100 |
| | 1B4–2 | 0.010 | 0.005 | 0.005 | 991 | -29 | 1120 |
| H + UM | 3B3–4 | 0.002 | 0.002 | 0.000 | 375 | 6 | 495,920 |
| | 3B2–4 | 0.002 | 0.002 | 0.000 | 382 | 2 | 431,912 |
| | 3B1–1 | 0.003 | 0.003 | 0.000 | 584 | -12 | 103,160 |
| | 3B2–2 | 0.003 | 0.003 | 0.000 | 609 | 27 | 80,374 |
| | 3B3–2 | 0.003 | 0.003 | 0.000 | 580 | 18 | 123,368 |
| | 3B1–2 | 0.005 | 0.004 | 0.001 | 845 | 12 | 10,076 |
| | 3B3–1 | 0.005 | 0.004 | 0.001 | 857 | -8 | 11,070 |
| | 3B5–1 | 0.005 | 0.004 | 0.001 | 862 | -30 | 11,624 |
| | 3B4–2 | 0.010 | 0.005 | 0.005 | 964 | -19 | 1410 |
| | 3B5–2 | 0.010 | 0.005 | 0.005 | 973 | -25 | 1250 |
| | 3B6–2 | 0.010 | 0.005 | 0.005 | 974 | -23 | 1382 |
| NH + UM | 2B6–4 | 0.002 | 0.002 | 0.000 | 344 | 0 | 1,212,970 |
| | 2B5–4 | 0.002 | 0.002 | 0.000 | 332 | -1 | 1,260,794 |
| | 2B1–2 | 0.003 | 0.003 | 0.000 | 503 | 5 | 133,400 |
| | 2B2–2 | 0.003 | 0.003 | 0.000 | 502 | -4 | 217,400 |
| | 2B4–3 | 0.003 | 0.003 | 0.000 | 521 | -9 | 93,560 |
| | 2B3–2 | 0.005 | 0.005 | 0.000 | 800 | 28 | 14,660 |
| | 2B2–4 | 0.005 | 0.005 | 0.000 | 819 | -10 | 18,774 |
| | 2B3–4 | 0.005 | 0.005 | 0.000 | 813 | 31 | 15,252 |
| | 2B5–2 | 0.010 | 0.006 | 0.004 | 958 | -28 | 1170 |
| | 2B1–4 | 0.010 | 0.006 | 0.004 | 985 | -1 | 1346 |
| | 2B6–2 | 0.010 | 0.006 | 0.004 | 979 | -14 | 1424 |

**Table 7**
Uniaxial, fully-reversed fatigue test results for L-PBF IN718 TW specimens with t = 1.25 mm.

| | Spec. ID | $\varepsilon_a$ (mm/mm) | $\Delta\varepsilon_e/2$ (mm/mm) | $\Delta\varepsilon_p/2$ (mm/mm) | $\sigma_a$ (MPa) | $\sigma_m$ (MPa) | $2 N_f$ |
|---|---|---|---|---|---|---|---|
| H + M | 1C5–3 | 0.002 | 0.002 | 0.000 | 395 | -4 | 7334,960 |
| | 1C6–3 | 0.002 | 0.002 | 0.000 | 399 | 0 | 3319,680 |
| | 1C1–1 | 0.003 | 0.003 | 0.000 | 563 | -1 | 174,626 |
| | 1C6–1 | 0.003 | 0.003 | 0.000 | 600 | -2 | 160,066 |
| | 1C4–2 | 0.003 | 0.003 | 0.000 | 611 | 3 | 184,902 |
| | 1C2–1 | 0.005 | 0.004 | 0.001 | 835 | -9 | 15,020 |
| | 1C3–1 | 0.005 | 0.004 | 0.001 | 871 | 43 | 14,708 |
| | 1C5–2 | 0.005 | 0.004 | 0.001 | 860 | -33 | 20,360 |
| | 1C1–2 | 0.010 | 0.005 | 0.005 | 990 | -28 | 1822 |
| | 1C2–2 | 0.010 | 0.005 | 0.005 | 988 | -30 | 1666 |
| | 1C3–2 | 0.010 | 0.005 | 0.005 | 984 | -31 | 2102 |
| H + UM | 3C2–3 | 0.002 | 0.002 | 0.000 | 390 | -5 | 3338,498 |
| | 3C4–3 | 0.002 | 0.002 | 0.000 | 394 | 3 | 3824,640 |
| | 3C4–1 | 0.003 | 0.003 | 0.000 | 591 | -4 | 129,156 |
| | 3C3–1 | 0.003 | 0.003 | 0.000 | 601 | 17 | 104,152 |
| | 3C1–2 | 0.003 | 0.003 | 0.000 | 603 | 13 | 66,432 |
| | 3C1–1 | 0.005 | 0.004 | 0.001 | 820 | -20 | 12,400 |
| | 3C5–1 | 0.005 | 0.004 | 0.001 | 859 | 11 | 8324 |
| | 3C3–2 | 0.005 | 0.004 | 0.001 | 853 | -26 | 12,200 |
| | 3C3–3 | 0.010 | 0.005 | 0.005 | 978 | -27 | 1206 |
| | 3C2–2 | 0.010 | 0.005 | 0.005 | 979 | -29 | 1208 |
| | 3C4–2 | 0.010 | 0.005 | 0.005 | 980 | -23 | 1496 |
| NH + UM | 2C1–4 | 0.002 | 0.002 | 0.000 | 331 | 4 | 1407,394 |
| | 2C3–4 | 0.002 | 0.002 | 0.000 | 338 | 11 | 1102,712 |
| | 2C1–2 | 0.003 | 0.003 | 0.000 | 499 | -3 | 183,524 |
| | 2C2–2 | 0.003 | 0.003 | 0.000 | 520 | -3 | 147,152 |
| | 2C4–3 | 0.003 | 0.003 | 0.000 | 535 | -21 | 219,058 |
| | 2C3–2 | 0.005 | 0.005 | 0.000 | 853 | -9 | 19,680 |
| | 2C4–2 | 0.005 | 0.005 | 0.000 | 817 | -31 | 21,900 |
| | 2C1–3 | 0.005 | 0.005 | 0.000 | 814 | -11 | 19,326 |
| | 2C5–2 | 0.010 | 0.006 | 0.004 | 990 | -26 | 1640 |
| | 2C2–4 | 0.010 | 0.006 | 0.004 | 1014 | -16 | 1068 |
| | 2C6–2 | 0.010 | 0.006 | 0.004 | 989 | -24 | 1566 |

**Table 8**
Uniaxial, fully-reversed fatigue test results for L-PBF IN718 NFC specimens with t = 1 mm (ID = 5 mm).

| | Spec ID | $\varepsilon_a$ (mm/mm) | $\Delta\varepsilon_e/2$ (mm/mm) | $\Delta\varepsilon_p/2$ (mm/mm) | $\sigma_a$ (MPa) | $\sigma_m$ (MPa) | $2 N_f$ |
|---|---|---|---|---|---|---|---|
| H + M | 1F1–2 | 0.002 | 0.002 | 0.000 | 391 | 2 | 845,136 |
| | 1F3–3 | 0.002 | 0.002 | 0.000 | 398 | 0 | > 10,000,000 |
| | 1F6–1 | 0.003 | 0.003 | 0.000 | 599 | 0 | 298,658 |
| | 1F8–1 | 0.003 | 0.003 | 0.000 | 599 | -6 | 248,246 |
| | 1F7–2 | 0.003 | 0.003 | 0.000 | 609 | 8 | 203,432 |
| | 1F3–1 | 0.005 | 0.004 | 0.001 | 832 | -25 | 20,422 |
| | 1F5–1 | 0.005 | 0.004 | 0.001 | 840 | -20 | 21,038 |
| | 1F5–3 | 0.005 | 0.004 | 0.001 | 853 | -52 | 14,870 |
| | 1F4–1 | 0.010 | 0.005 | 0.005 | 982 | -26 | 2630 |
| | 1F7–1 | 0.010 | 0.006 | 0.005 | 966 | -48 | 3002 |
| | 1F2–2 | 0.010 | 0.005 | 0.005 | 989 | -30 | 1956 |
| H + UM | 3F3–3 | 0.002 | 0.002 | 0.000 | 380 | 0 | 1031,248 |
| | 3F7–3 | 0.002 | 0.002 | 0.000 | 384 | 1 | 1565,412 |
| | 3F4–1 | 0.003 | 0.003 | 0.000 | 604 | -9 | 103,704 |
| | 3F6–1 | 0.003 | 0.003 | 0.000 | 599 | 0 | 92,600 |
| | 3F8–2 | 0.003 | 0.003 | 0.000 | 605 | -5 | 227,608 |
| | 3F3–1 | 0.005 | 0.004 | 0.001 | 855 | -18 | 12,806 |
| | 3F5–1 | 0.005 | 0.004 | 0.001 | 824 | -14 | 11,316 |
| | 3F1–3 | 0.005 | 0.004 | 0.001 | 811 | -27 | 14,576 |
| | 3F1–1 | 0.010 | 0.005 | 0.005 | 984 | -29 | 1560 |
| | 3F2–1 | 0.010 | 0.005 | 0.005 | 982 | -32 | 1460 |
| | 3F3–2 | 0.010 | 0.005 | 0.005 | 948 | -28 | 1708 |
| NH + UM | 2F6–3 | 0.002 | 0.002 | 0.000 | 349 | 2 | 791,876 |
| | 2F7–3 | 0.002 | 0.002 | 0.000 | 340 | -2 | 1306,402 |
| | 2F1–2 | 0.003 | 0.003 | 0.000 | 560 | -8 | 224,644 |
| | 2F3–2 | 0.003 | 0.003 | 0.000 | 544 | -2 | 210,010 |
| | 2F2–3 | 0.003 | 0.003 | 0.000 | 509 | 0 | 282,078 |
| | 2F4–2 | 0.005 | 0.005 | 0.000 | 794 | -30 | 29,528 |
| | 2F5–2 | 0.005 | 0.005 | 0.000 | 828 | -28 | 23,136 |
| | 2F3–3 | 0.005 | 0.005 | 0.000 | 790 | -13 | 22,768 |
| | 2F6–2 | 0.010 | 0.006 | 0.004 | 963 | -25 | 1740 |
| | 2F7–2 | 0.010 | 0.006 | 0.004 | 948 | -28 | 2040 |
| | 2F4–3 | 0.010 | 0.006 | 0.004 | 955 | -22 | 1706 |

**Table 9**
Uniaxial, fully-reversed fatigue test results for L-PBF IN718 NFC specimens with t = 2.5 mm (ID = 2 mm).

|          | Spec ID | $\varepsilon_a$ | $\Delta\varepsilon_e/2$ | $\Delta\varepsilon_p/2$ | $\sigma_a$ (MPa) | $\sigma_m$ (MPa) | 2 $N_f$ |
|----------|---------|-------|-------|-------|-------|-------|-----------|
| H + M    | 1D3–3   | 0.002 | 0.002 | 0.000 | 393 | 0   | 788,240 |
|          | 1D1–3   | 0.002 | 0.002 | 0.000 | 404 | 24  | 889,308 |
|          | 1D3–1   | 0.003 | 0.003 | 0.000 | 609 | 3   | 332,000 |
|          | 1D5–1   | 0.003 | 0.003 | 0.000 | 601 | -13 | 462,832 |
|          | 1D4–2   | 0.003 | 0.003 | 0.000 | 599 | 8   | 341,484 |
|          | 1D4–1   | 0.005 | 0.004 | 0.001 | 847 | -28 | 19,114 |
|          | 1D6–1   | 0.005 | 0.004 | 0.001 | 827 | -27 | 23,102 |
|          | 1D5–2   | 0.005 | 0.004 | 0.001 | 841 | -44 | 17,354 |
|          | 1D7–1   | 0.010 | 0.005 | 0.005 | 973 | -27 | 2028 |
|          | 1D8–1   | 0.010 | 0.005 | 0.005 | 971 | -27 | 2382 |
|          | 1D3–2   | 0.010 | 0.005 | 0.005 | 959 | -29 | 2836 |
| H + UM   | 3D3–2   | 0.002 | 0.002 | 0.000 | 397 | -1  | 4177,394 |
|          | 3D3–3   | 0.002 | 0.002 | 0.000 | 399 | -3  | 1013,704 |
|          | 3D4–1   | 0.003 | 0.003 | 0.000 | 597 | -6  | 215,906 |
|          | 3D5–1   | 0.003 | 0.003 | 0.000 | 600 | -4  | 212,172 |
|          | 3D2–2   | 0.003 | 0.003 | 0.000 | 611 | -7  | 266,046 |
|          | 3D3–1   | 0.005 | 0.004 | 0.001 | 819 | -38 | 21,000 |
|          | 3D8–1   | 0.005 | 0.004 | 0.001 | 818 | -28 | 18,144 |
|          | 3D4–2   | 0.005 | 0.004 | 0.001 | 834 | -38 | 19,484 |
|          | 3D6–1   | 0.010 | 0.005 | 0.005 | 971 | -27 | 3040 |
|          | 3D7–1   | 0.010 | 0.005 | 0.005 | 949 | -24 | 2440 |
|          | 3D8–2   | 0.010 | 0.005 | 0.005 | 962 | -30 | 2718 |
| NH + UM  | 2D1–3   | 0.002 | 0.002 | 0.000 | 367 | 0   | 1624,910 |
|          | 2D8–3   | 0.002 | 0.002 | 0.000 | 374 | -1  | 2627,714 |
|          | 2D3–2   | 0.003 | 0.003 | 0.000 | 598 | -15 | 313,402 |
|          | 2D6–3   | 0.003 | 0.003 | 0.000 | 545 | 11  | 288,288 |
|          | 2D4–2   | 0.003 | 0.003 | 0.000 | 585 | 0   | 273,250 |
|          | 2D5–2   | 0.005 | 0.005 | 0.000 | 852 | -23 | 30,666 |
|          | 2D6–2   | 0.005 | 0.005 | 0.000 | 846 | -30 | 33,728 |
|          | 2D2–3   | 0.005 | 0.005 | 0.000 | 852 | -23 | 32,088 |
|          | 2D7–2   | 0.010 | 0.006 | 0.004 | 958 | -24 | 2120 |
|          | 2D8–2   | 0.010 | 0.006 | 0.005 | 973 | -32 | 2580 |
|          | 2D5–3   | 0.010 | 0.006 | 0.004 | 982 | -30 | 2712 |

Strain-life plots exhibiting the effects of different post-processing conditions (i.e., H + M, H + UM, and NH + UM) for three TW and two NFC geometries are presented in Fig. 7. In the case of TW specimens (see Fig. 7(a)-(c)), the effect of surface condition on the fatigue life was not significant. H + M specimens showed similar fatigue lives as compared to the H + UM and NH + UM specimens. This behavior was consistent across all the thicknesses of TW geometries. The effect of HIP was noticed in TW geometries under certain conditions. For instance, the TW NH + UM specimens with t = 0.50 mm tested at $\varepsilon_a$ = 0.002 mm/mm had slightly longer fatigue lives than HIP ones. However, opposite trend was noticed for specimens with t = 1.25 mm at $\varepsilon_a$ = 0.002 mm/mm, where H + M and H + UM specimens exhibited better fatigue resistance compared to NH + UM ones. NFC specimens (see Fig. 7(d)-(e)) showed similar behavior, where the effect of surface condition and HIP on fatigue lives was insignificant in all fatigue regimes. This behavior was consistent for both t = 1 and 2.5 mm specimens.

The strain-life fatigue plots exhibiting the effect of specimen wall thicknesses on the fatigue life of TW and NFC specimens are shown in Fig. 8. For TW geometry in the H + M and H + UM conditions, although the effect of thickness on fatigue life was not considerable at $\varepsilon_a$ = 0.010, 0.003, and 0.005 mm/mm amplitudes (see Fig. 8(a)-(c)), fatigue life was observed to increase with an increase in thickness at $\varepsilon_a$ = 0.002 mm/ mm with the most noticeable trend being in H + M condition. Unlike TW geometries, the effect of thickness on fatigue lives was not observed at any of NFC specimens (see Fig. 8(d)-(f)). In LCF to MCF regime (including tests at $\varepsilon_a \geq$ 0.003 mm/mm), the difference in fatigue lives between 1 and 2.5 mm thick NFC specimens under different conditions was less than a factor of 2, which is insignificant considering the scattered nature of fatigue data. In the HCF regime, where the scatter in fatigue lives was larger, the differences between 1 and 2.5 mm NFC specimens were even less noticeable.

## 4. Discussion

### 4.1. Role of microstructure and specimen wall thickness on tensile behavior

A slightly higher YS of NonHIP specimens (by ~100 MPa or ~10%) compared to HIP counterparts for both NFC and TW geometries is associated with the difference in the microstructure. As presented in Fig. 2(c), the NonHIP specimens possessed finer grain structure compared to HIP ones (see Fig. 2(f)) permitting much shorter dislocation pileups. The larger population of δ precipitates and remnant dendritic microstructure in NonHIP specimens (see Fig. 2(c)) can further limit the free slip distance [36]. Indeed, Gallmeyer et al. [37] in a systematic study on L-PBF IN718 showed that the strengthening effect from the dendritic microstructure can be more pronounced than grain size strengthening. According to the Hall-Petch relationship [38], YS is inversely proportional to the square root of dislocation pileup length, which explains the noticeably higher yield strengths of the NonHIP specimens.

Overall, EL is typically governed by the specific fracture mechanism, which depended on microstructure (e.g., brittle phase), surface condition specimen wall thickness. To better understand why HIP specimens showed better EL compared to NonHIP ones, BSE images taken from the longitudinal plane (parallel to the build direction) of fractured specimens are shown in Fig. 9. For a fair comparison and explanation, identical internal surface conditions were considered, which are H + UM and NH + UM. In the case of NH + UM specimens (see Fig. 9(a) & (b)), a large population of closely spaced δ particles were present. It is well known that the δ phase's brittleness and relatively large size encourage crack opening by either interface decohesion or particle fracture [39]. An example of a crack opening after δ particle fracture is shown in Fig. 9(b), where a particle-matrix debonding event is also indicated by the lower right arrow. The closely spaced δ particles along
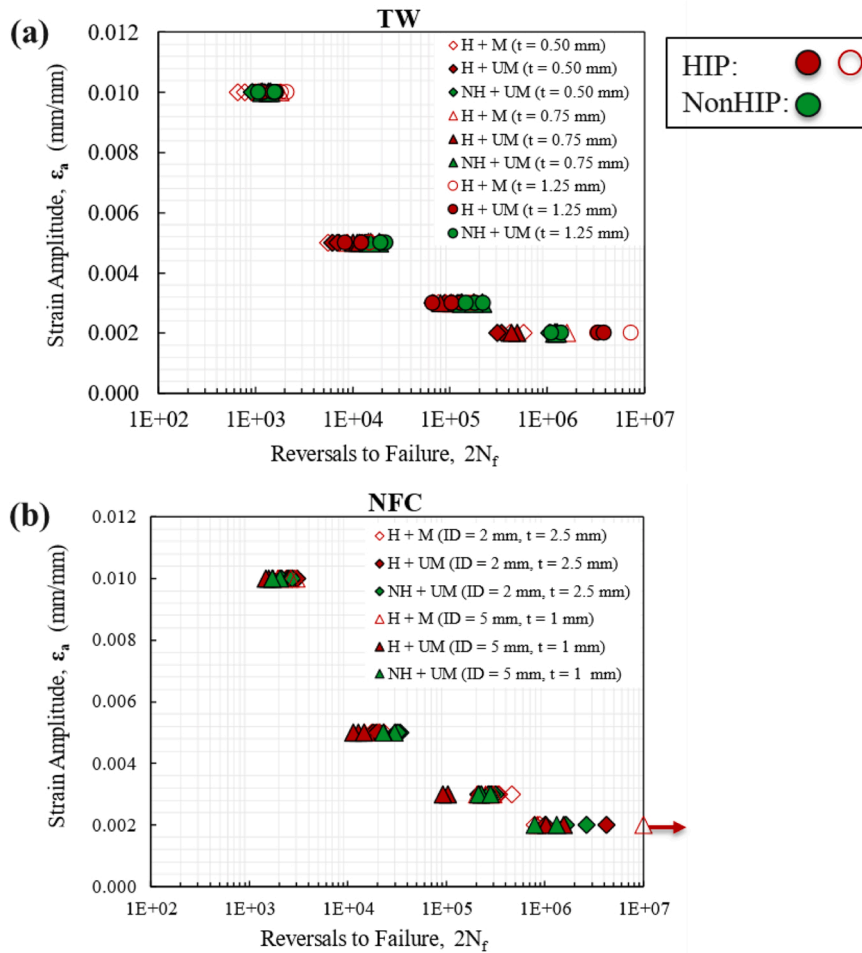
**Fig. 6.** Strain-life fatigue behavior of L-PBF IN718 in the HIP (shown using red symbols) and NonHIP conditions (shown using green symbols): (a) TW specimens and (b) NFC specimens.
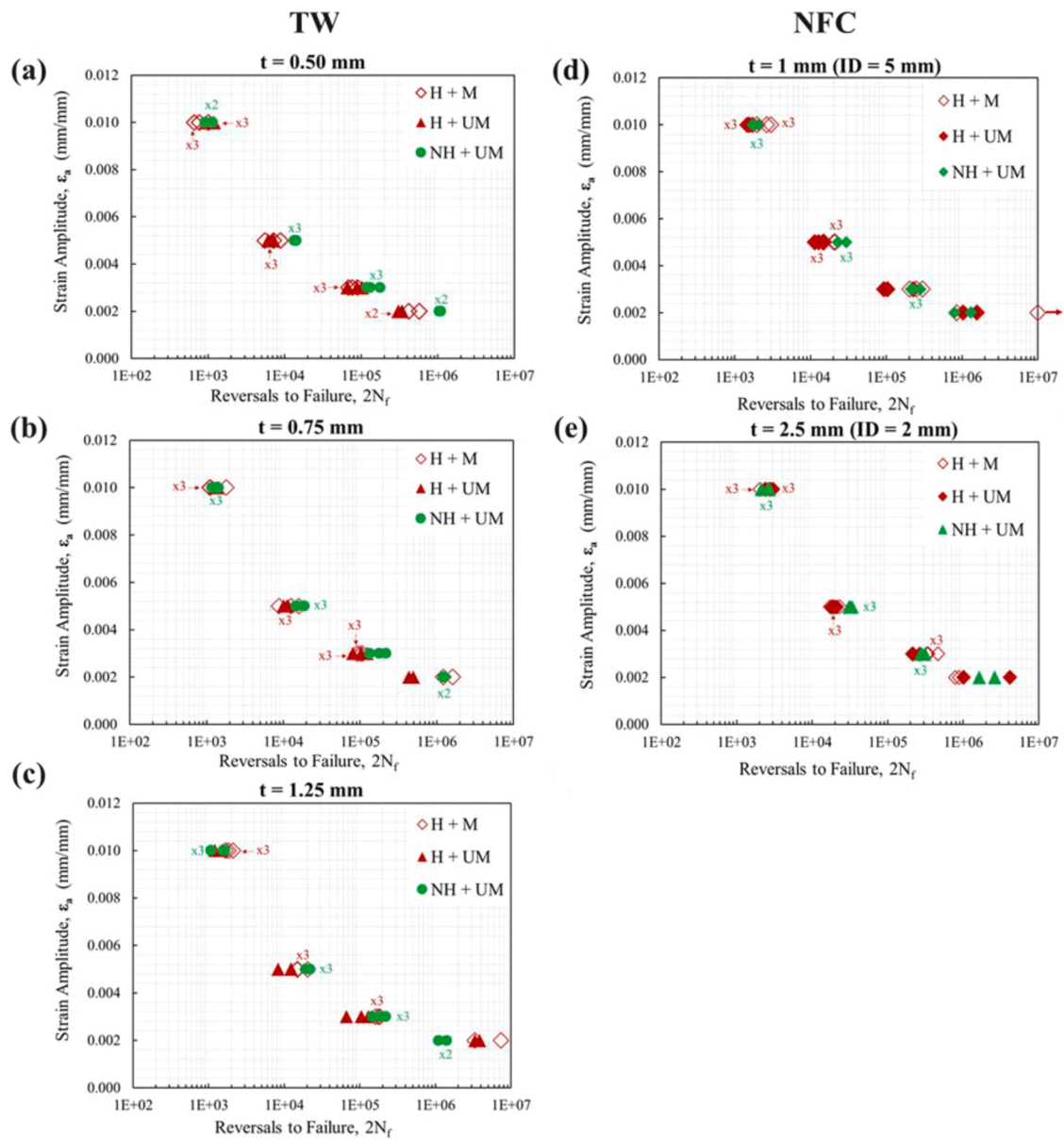
**Fig. 7.** Strain-life fatigue results demonstrating the effects of different post-processing conditions on the fatigue life for L-PBF IN718 specimens of different thicknesses: (a) TW t = 0.50 mm, (b) TW t = 0.75 mm, (c) TW t = 1.25 mm, (d) NFC t = 1 mm, and (e) NFC t = 2.5 mm.
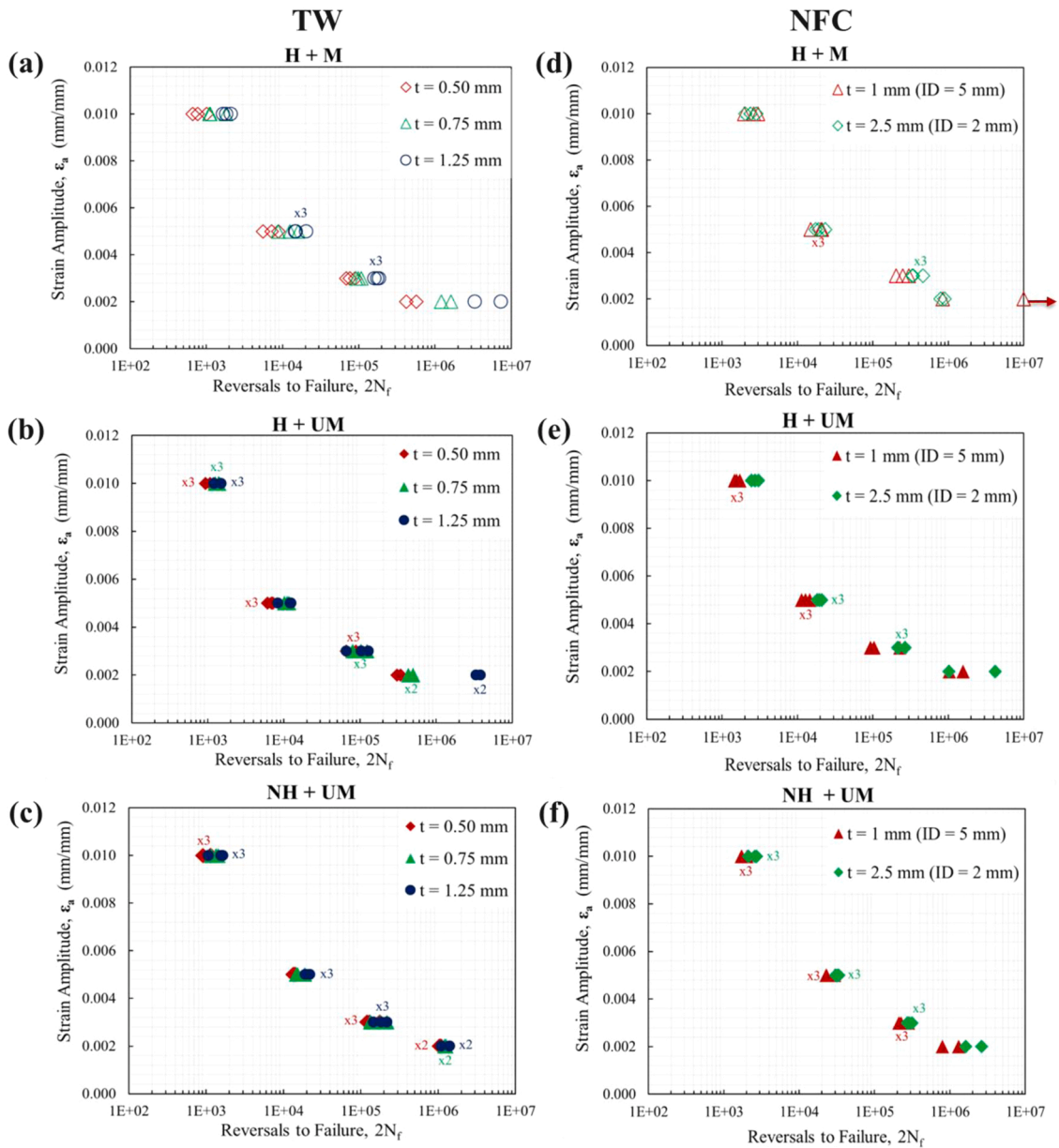
**Fig. 8.** Strain-life fatigue results of L-PBF IN718 specimens showing the effect of wall thickness on fatigue life for different post-processing condition: (a) TW H + M, (b) TW H + UM, (c) TW NH + UM, (d) NFC H + M, (e) NFC H + UM, and (f) NFC NH + UM.

the grain boundaries and within grains provided abundant sites for void nucleation, leading to early onset of fracture and reduced EL. On the other hand, in the case of H + UM specimens, carbide debonding from the matrix governed the fracture due to the significantly lower δ phase fraction (see Fig. 9(c) & (d)). However, even though the population of the carbides were larger than that of δ precipitates in the HIP microstructure, it was still substantially lower than δ precipitate population in the NonHIP one [40]. The lack of void nucleation sites delayed the fracture and encouraged HIP specimens to elongate more than NonHIP ones.

The higher EL observed in thicker TW and NFC specimens can be explained using the general relationship between thickness and fracture toughness schematically shown in Fig. 10(a). This relationship suggests that when the fracture mode is purely plane stress—i.e., the fracture is governed by shear—larger wall thickness results in higher toughness (see the shear fracture regime in Fig. 10(a)) and delayed fracture. To illustrate, tensile fracture surfaces of the NFC specimens in H + M condition are shown in Fig. 10(b)-(d) and Fig. 10(e)-(g). The entire

fracture surfaces were shear (i.e., Regime I in Fig. 10(a)) induced as evidenced by their 45° angle from the loading direction (examples are shown in Fig. 10(b) & (e)). Confirmed by the purely shear mode fracture surfaces, the state of stress of the fracture of NFC H + M specimens was plane stress [41]. Thus, specimens with thicker walls possessed higher toughness which delayed the onset of fracture in the H + M NFC and TW specimens, and hence, improved ductility.

In contrast, the trend of increasing EL with increasing thickness was greatly suppressed, or in some cases completely not observed, for TW and NFC specimens with unmachined surfaces. To explain this, fracture surfaces of NH + UM NFC specimens with thickness t = 1 mm, and t = 2.5 mm are presented in Fig. 10(h)-(j) and Fig. 10(k)-(m), respectively. Unlike the H + M specimens, these fracture surfaces clearly contained flat regions and shear lips (Regime II in Fig. 10(a)), indicating brittle failure and the stress state deviating from purely plane stress. Higher magnification images (see Fig. 10(j) & (m)) indicate that cracks initiated primarily from the ID, suggesting that as-built surface notches induced crack initiation and subsequent failure. The so-initiated cracks,
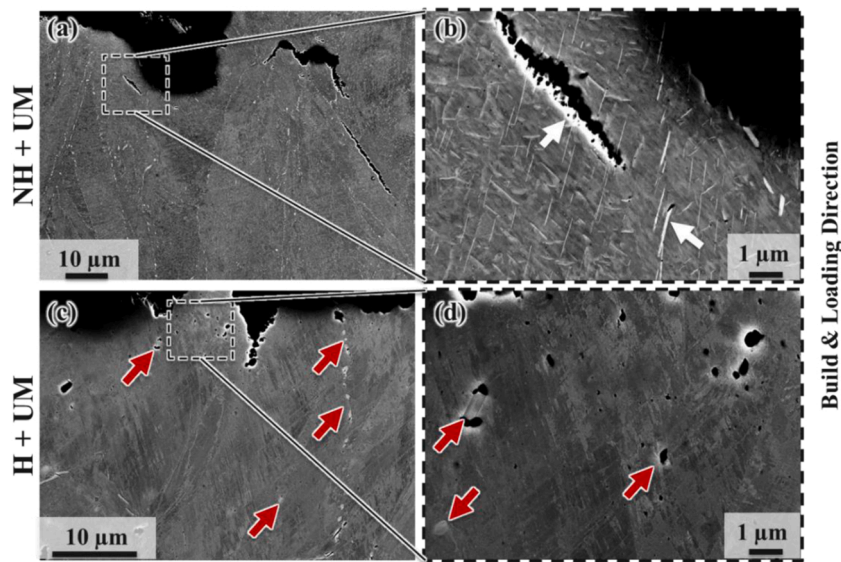
**Fig. 9.** BSE micrographs obtained from the longitudinal plane of NFC specimens in different post-processing conditions: (a)-(b) NH + UM and (c)-(d) H + UM. Red and white arrows indicate debonded carbides and δ particles, respectively.

whose propagation direction was through the wall thickness (as evidenced by the flat portion of the fracture surfaces shown in Fig. 10(j) & (m)), had longer lengths compared to circumferentially propagating ones (i.e., the tearing mode seen in Fig. 10(b) & (e)), were in-effect in plane strain condition, and corresponded to lower fracture toughness and lower EL. Therefore, the trend of higher EL with larger thickness for H + M specimens (see Fig. 5(d)) vanished under the NH + UM condition (see Fig. 5(f). Compared to NH + UM specimens, the HIP microstructure of the H + UM ones was significantly coarsened, mostly rid of the detrimental δ precipitates, and less sensitive to surface notches. As a result, higher EL values at larger thickness were still somewhat visible in the H + UM NFC specimens.

The variations in the fracture mechanisms of H + M, to H + UM, and to NH + UM conditions observed for the NFC specimens were also valid for the TW specimens. In fact, the fracture surfaces of all the H + M and H + UM TW specimens formed 45° angles with the loading direction, which indicated completely plane stress state and resulted in more pronounced thickness effect on EL (see Fig. 5(a)-(c)).

### 4.2. Effects of post-processing and specimen wall thickness on LCF and MCF life

The fatigue behaviors of NFC and TW specimens were insensitive to post-processing (i.e., HIP and machining) and wall thickness in LCF and MCF regimes (i.e., $\varepsilon_a = 0.010$, 0.005, and 0.003 mm/mm) as shown in Fig. 7 and Fig. 8. Indeed, as shown in both figures, the differences in fatigue lives among specimens under different conditions at these strain amplitudes were less than a factor of 2, which was insufficient to draw any conclusions on the effect of post-processing and thickness. Knowing that the fatigue crack growth phase typically occupies large portions of fatigue lives in LCF regime and that the stable crack growth in IN718 is not strongly influenced by the changes in microstructure (such as grain size) [43], the insensitivity at higher strain amplitudes—such as 0.005 and 0.010 mm/mm— was expected.

To verify the dominance of crack growth in the LCF regime, NFC specimens loaded to 25% and 50% of the average expected fatigue life under 0.010 mm/mm strain amplitude were examined non-destructively (both optical and XCT methods) for presence of cracks on the ID and OD surfaces. Two longitudinal cross sections of an NFC specimen (t = 2.5 mm H + UM), cyclically loaded until 50% of the average expected fatigue life, from XCT scans are shown in Fig. 11. White arrows indicate the presence of several cracks, with lengths ranging from 50 μm to 300 μm, at the ID surface.

Cracks were also observed with optical microscope (Keyence VHX-6000) on the OD surface of the gage in partially fatigued specimens as shown in Fig. 12. On the undeformed specimen, there were no cracks visible except for several machining marks present on the surface. After being subjected to cyclic loading of 25% of the average expected fatigue life at the 0.010 mm/mm strain amplitude, several cracks with lengths ranging from 50 to 100 μm appeared on the OD surfaces of the specimens, which implies that crack initiated even before reaching 25% of life. Upon loading up to 50% of the expected fatigue life, cracks grew up to 300 μm. The observations made here indicated that cracks initiated in very early stages of fatigue life in LCF regime; therefore, crack propagation occupied a major portion of fatigue life.

Compared to the LCF regime, the initiation phase of fatigue cracks tends to become more important in the MCF regime. Nevertheless, the insensitivity of fatigue life to changes in either microstructure or surface condition at the 0.003 mm/mm amplitude (see Fig. 7) may suggest that (a) the crack initiation life of IN718 was not significantly affected by such changes in the MCF regime, and/or (b) crack growth still dominated fatigue life under this strain amplitude. The first hypothesis was somewhat confirmed by the observations made earlier on the 50% fatigued NFC specimens at 0.010 mm/mm that the crack lengths on the ID unmachined surface (Fig. 11) and OD machined/polished surface (Fig. 12) were consistent, indicating equal tendency of crack initiation at both locations despite the significantly different surface conditions.

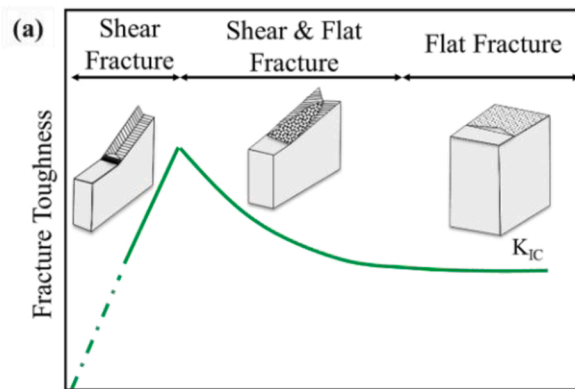The second hypothesis was supported by the fact that the multiple

**Fig. 10.** (a) Schematic illustration of fracture toughness as a function of thickness [42]. (b)-(m) Tensile fracture surfaces of the NFC specimens with different thicknesses: (b)-(d) t = 1 mm H + M, (e)-(g) t = 2.5 mm H + M, (h)-(j) t = 1 mm NH + UM, (k)-(m) t = 2.5 mm NH + UM. (b), (e), (h), and (k) show the isometric views of fracture surfaces, while (c), (f), (i) and (l) exhibit top views. Enclosed areas in (i) and (l) represent flat regions. Red arrow in (h) points at the flat region, while red ellipse in (j) and (m) indicates notch.
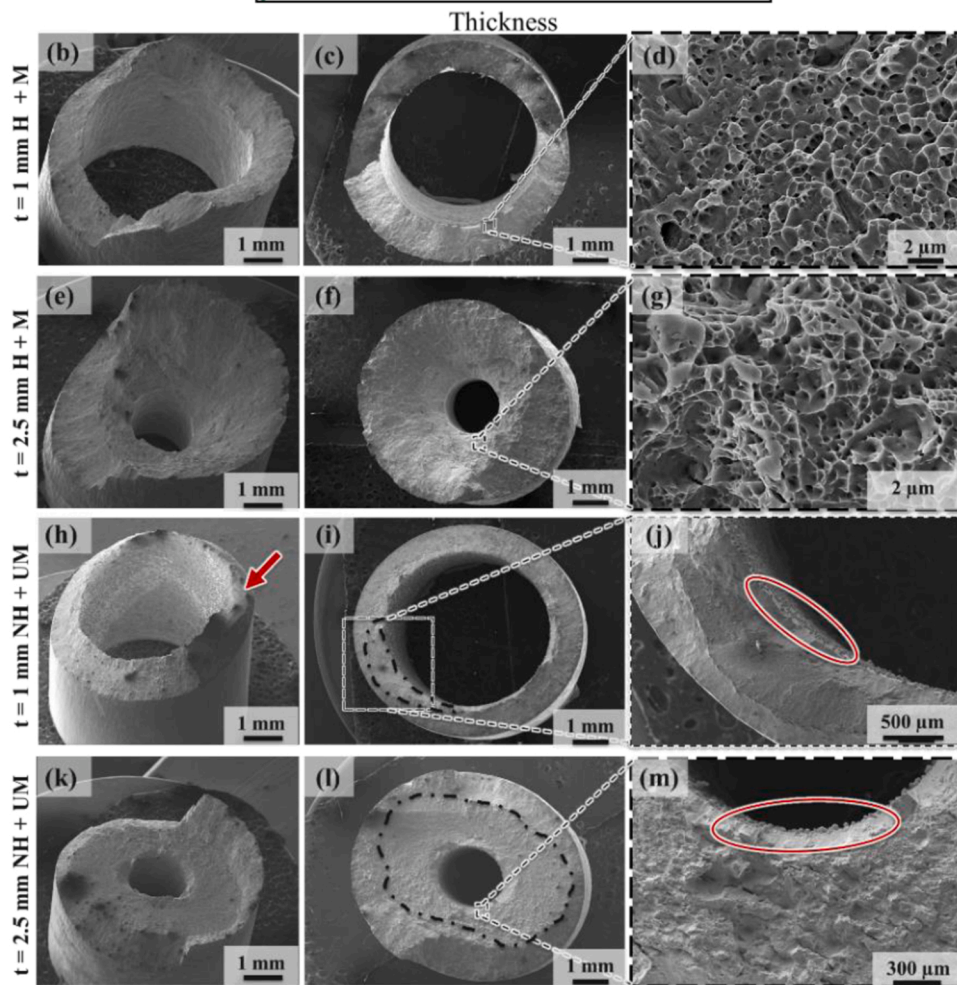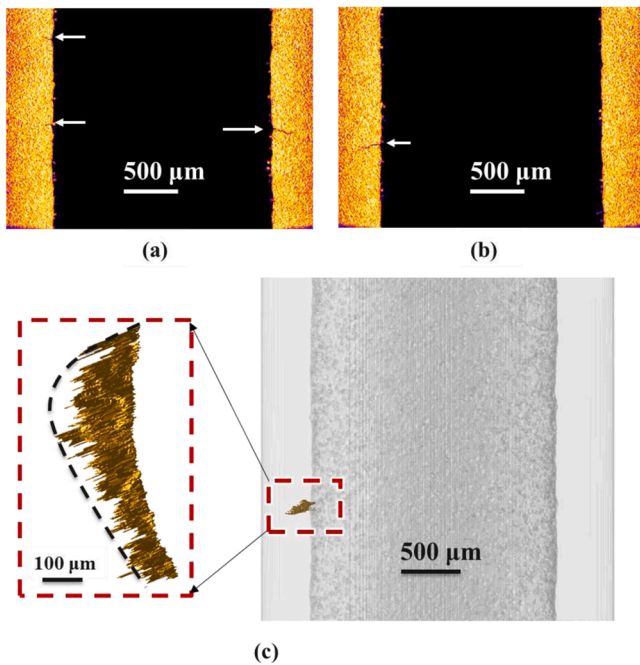
**Fig. 11.** High-resolution (voxel size ~3 μm) XCT results showing cracks at the ID surface of an NFC specimen (t = 2.5 mm H + UM). White arrows point to multiple cracks on the same specimen. Note that specimen was tested at $\varepsilon_a$ = 0.010 mm/mm up to 50% of the expected fatigue life. One of the fatigue cracks shown is rendered in 3D and presented in (c). Given the noise in the data, the true crack front could not be determined but was schematically shown using a black dashed line.

crack initiation sites were observed on the fracture surface of each specimen tested at 0.003 mm/mm strain amplitude. For instance, the fracture surfaces obtained from some H + M NFC specimens with t = 2.5 mm (2 $N_f$ = 332,000 reversals) and t = 1 mm (2 $N_f$ = 298,658 reversals) tested at 0.003 mm/mm strain amplitude are presented in the Fig. 13(a) & (b). Fatigue cracks were observed to initiate from multiple locations indicated by red and white arrows (see Fig. 13(a) & (b)). Fatigue cracks originated mainly from the machining marks on the ID surfaces and from PSBs (as evidenced by the presence of crystallographic facets on the fracture surfaces) on OD surfaces and sub-surfaces, and not from any volumetric defects such as lack of fusion and gas-entrapped pores in other materials as reported by Refs. [44–46]. Although there were several crack initiations sites, in some cases, initiation from the OD was more critical, such as the one shown in Fig. 13(a). In general, for all specimens fractured at 0.010, 0.005, and 0.003 mm/mm strain amplitudes, regardless of surface and HT conditions, multiple crack initiations from both ID and OD of the specimens were always observed. Even in the ID unmachined and OD machined condition, where the ID surface was much more favorable for crack initiation, multiple cracks could be seen initiated from the machined OD surface. An example of this for TW specimens is provided in Fig. 13(c), the same observations were also made for NFC specimens.

The presence of multiple crack initiation sites on a fracture surface indicates strong crack growth resistance which could slow the growth of each crack and permit time for the initiation/growth of other cracks [47]. As a result, the observation that multiple cracks initiated from ID and OD indicates that crack propagation was a major fraction of total life of IN718 specimens regardless of their surface and HT condition even in the MCF regime. Finally, as presented in Fig. 7, the fatigue lives of either TW or NFC specimens in the LCF and MCF regimes were not significantly affected by HIP or surface machining. Although crack initiation can be affected by surface roughness, no effect of surface roughness was noticeable in the LCF and MCF lives since they appeared to be

dominated by the crack growth stage. It could further be deduced that the growth rate of stable crack growth in IN718 should not be strongly affected by microstructural variations. On a similar vein, fatigue crack growth of IN718 typically has been found not to be strongly influenced by specimens' wall thickness. For instance, James [48] showed that specimen's thickness between 1.55 and 12.7 mm did not noticeably influence the stable crack growth rate of wrought IN718. Noting that in present study the specimens' wall thicknesses were ≤ 2.5 mm, fatigue lives were unaffected by changes in wall thickness in the LCF and MCF regimes. One possible reason could be significantly higher plastic deformation at the crack tip and large plastic zone size (i.e., planes stress) which prevented any effect of wall thickness on stable crack growth.

### 4.3. Effect of specimen wall thickness and post-processing on HCF behavior

Fatigue lives were observed to increase with increasing thickness for HIP TW specimens at $\varepsilon_a$ = 0.002 mm/mm, where fatigue lives were within HCF regime (see Fig. 8(a) & (b)). Here, unlike specimens tested at higher strain amplitudes, fatigue crack initiation dominated the fatigue life. Therefore, factors that could influence the fatigue crack initiation behavior were also expected to influence fatigue life.

The crack initiation regions on fracture surfaces of TW specimens of different thicknesses failed at $\varepsilon_a$ = 0.002 mm/mm are presented in Fig. 14. As evidenced by the prevalence of crystallographic facets, the crack initiation was clearly dominated by PSBs. Interestingly in HIP condition, cracks always initiated from sub-surface PSBs in the TW specimens (see Fig. 14(a), (b), (d), & (e)) even in the presence of as-built surface roughness. This was in contrast to the prior studies performed on solid cylindrical IN718 specimens with similar microstructure, where surface crack initiation was the governing fatigue failure mechanism [12,49]. This clear dominance of PSBs in the crack initiation was originated from the relatively few grains through the thicknesses of the HIP specimen walls— about 12–33 grains from the thinnest to the thickest walls as shown in Fig. 2(i). Comparing to bulk conditions (such as the ones seen in solid cylindrical specimens), the relatively few grains could impose less constrain to the operation of PSBs, and therefore, accelerated the fatigue crack initiation. The accelerated fatigue crack initiation permitted by thinner specimen walls was therefore responsible for the effect of wall thickness on fatigue life observed at $\varepsilon_a$ = 0.002 mm/mm for H + M and H + UM TW specimens (Fig. 8(a) & (b)); the thinner the wall thickness, the shorter the fatigue life.

In contrast, in the NonHIP, unmachined specimens, the surface notches competed with PSBs to initiate the crack; cracks mostly initiated from surface notches (e.g., see Fig. 14(f)), with the exception of t = 0.50 mm where initiations were from PSBs. The initiation from PSBs was again related to the relatively small grain count in the NH + UM t = 0.50 mm specimens which was not the case for the thicker NH + UM specimens. The effect of through-the-thickness grain count on fatigue life was also evident when the HCF lives of TW H + M, H + UM, and NH + UM specimens were compared at different thicknesses (Fig. 7(a)-(c)). Recall also from Fig. 7(a) that the fatigue lives of NH + UM specimens with t = 0.50 mm at $\varepsilon_a$ = 0.002 mm/mm were higher than the ones for the HIP counterparts (i.e., under H + M and H + UM conditions) by approximately a factor of 2. Noting that all three specimens types had fatigue crack initiation from PSBs at this wall thickness (Fig. 14(a)-(c)), the slightly higher fatigue lives of TW NH + UM specimens could be explained by more grains being present through the specimen wall thicknesses (see Fig. 2(i)). NH + UM finer grain size and the presence of high density δ precipitates (see Fig. 2(c)) resisted the formation of PSBs, and delayed the crack initiation [50].

In contrast, the TW NH + UM specimens with t = 1.25 mm had slightly shorter fatigue lives than their HIP (i.e., H + M and H + UM) counterparts at $\varepsilon_a$ = 0.002 mm/mm (see Fig. 7(c)). This change in the order of fatigue lives of NonHIP specimens with the increase in thickness
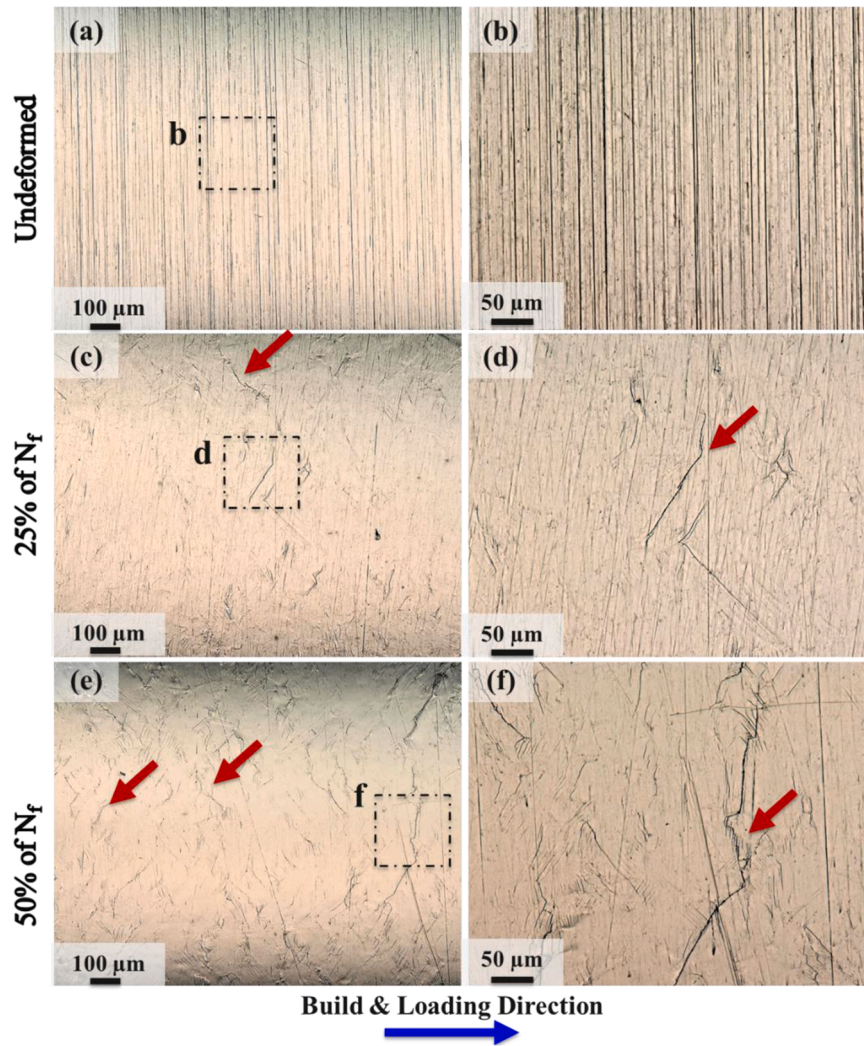
**Fig. 12.** Micrographs taken on the OD surfaces of an L-PBF IN718 NFC (t = 2.5 mm H + UM) specimen at different stages of cyclic loading with $\varepsilon_a$ = 0.010 mm/mm: (a)-(b) undeformed, (c)-(d), and (e)-(f) respectively at 25% and 50% of the expected fatigue life. Red arrows point to cracks.
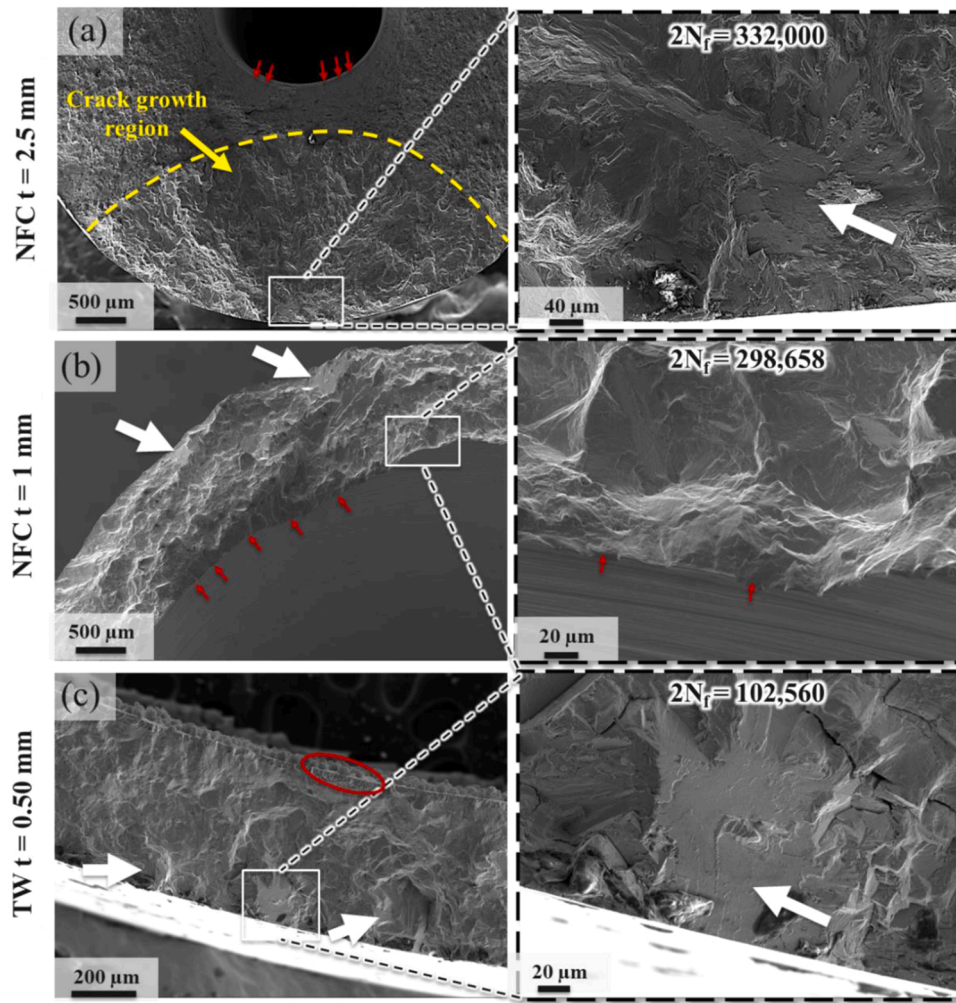
**Fig. 13.** Fatigue fracture surfaces for different thicknesses and surface conditions: (a) NFC t = 2.5 mm H + M, (b) NFC t = 1 mm H + M, and (c) TW t = 0.50 mm H + UM. Crack initiation sites from surface notch are indicated by red ellipses or red arrows. White arrows point at crystallographic facets. A crack growth region is demarcated using yellow dotted line in (a).

could be associated with an apparent transition of fatigue crack initiation mechanism. As shown in Fig. 14(f), cracks of TW NH + UM specimens with t = 1.25 mm always initiated from the as-built surface notches instead of PSBs. A transition in crack initiation behavior from PSBs to surface notches could also be attributed to higher number of finer grains through thickness (~ 50 grains as shown in Fig. 2(i)), suppressing the operation of PSBs.

Unlike TW HIP specimens, fatigue life of NFC HIP specimens did not increase with thickness at $\varepsilon_a$ = 0.002 mm/mm (see Fig. 8(d)-(f)). To explain, fracture surfaces of NFC specimens at $\varepsilon_a$ = 0.002 mm/mm are presented in Fig. 15. As shown by red ellipses in Fig. 15(a)-(f), surface notches mainly governed the crack initiation in NFC specimens— irrespective of HT condition. Interestingly, even when the ID surfaces were machined, cracks were still observed to initiate from the machining marks on the surface as shown in Fig. 15(a) & (d). One probable reason could be poor quality of internal machining and resultant surface machining grooves (see Fig. 3). Given the narrow ID of NFC specimens,

they were relatively challenging to machine. In some instances, powder particles could be seen attached to the ID surface indicating insufficient machining. Fig. 15(d) shows an instance of fatigue crack initiation from a deep as-built surface notch that was not removed during machining. Given that surface notch governed crack initiation in NFC specimens instead of PSB, the effects of specimen wall thickness and machining were not noticeable.

In both LCF and HCF regimes, fracture surfaces (see Figs. 13 to 15) indicated that multiple cracks were initiated mainly from the rough surfaces, machining marks, or PSBs and not from any volumetric defects (i.e., pores or lack of fusion). Also, crack initiation was due to plasticity in both regimes, which was profuse in LCF and more localized in HCF due to either near surface roughness or elastic incompatibility among grains. In addition, crack growth occupied a major portion of fatigue life in LCF and gradually became less important with decreasing strain levels. Its role became negligible in the HCF regime, where crack initiation was a major fraction of fatigue life.
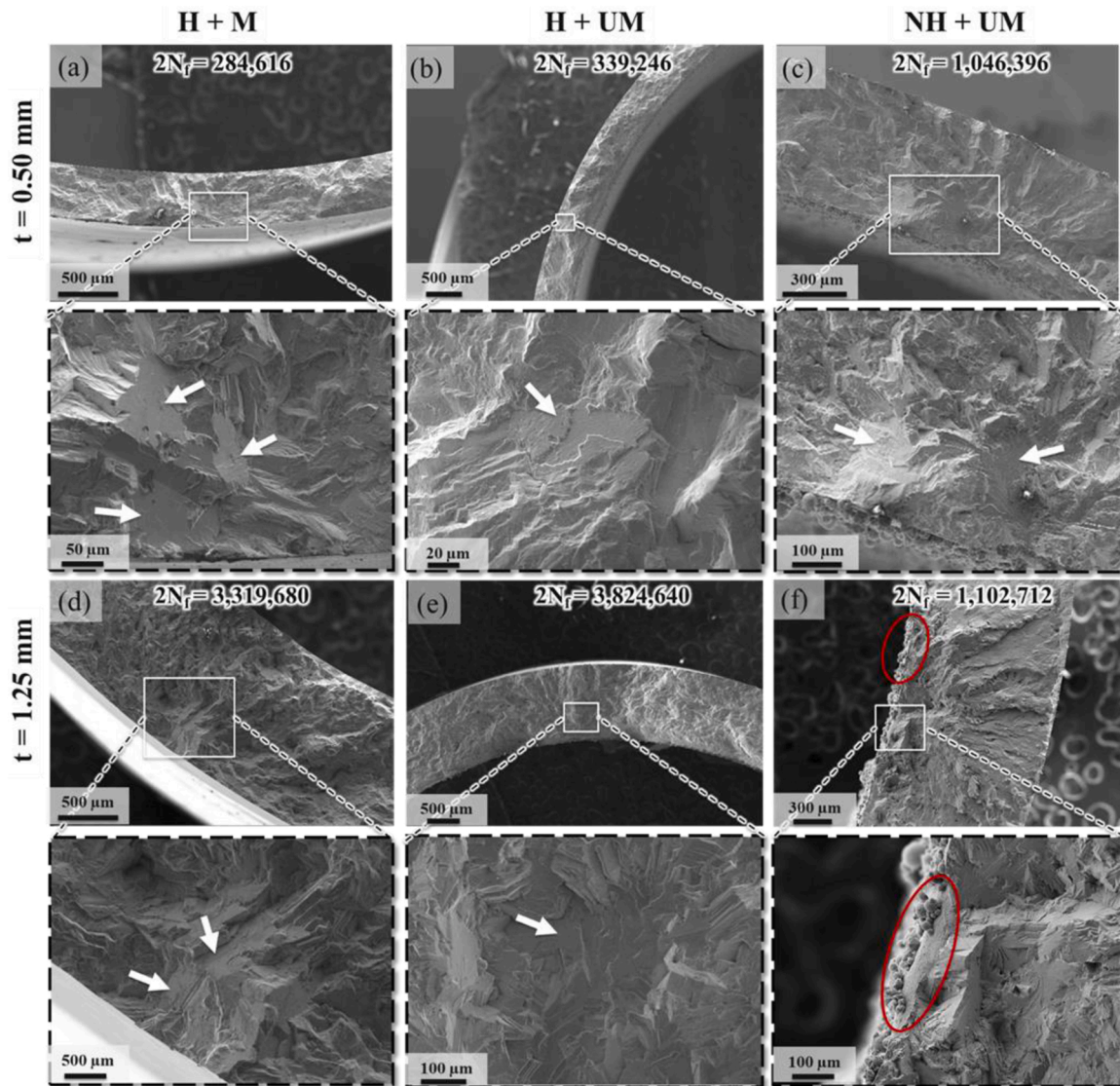
**Fig. 14.** Fatigue fracture surfaces of TW specimens with different thicknesses and post-processing conditions tested at $\varepsilon_a = 0.002$ mm/mm: (a) t = 0.50 mm H + M, (b) t = 0.50 mm H + UM, (c) t = 0.50 mm NH + UM, (d) t = 1.25 mm H + M, (e) t = 1.25 mm H + UM, and (f) t = 1.25 mm NH + UM. White arrows point at crystallographic facets, while red ellipses indicate surface notches.
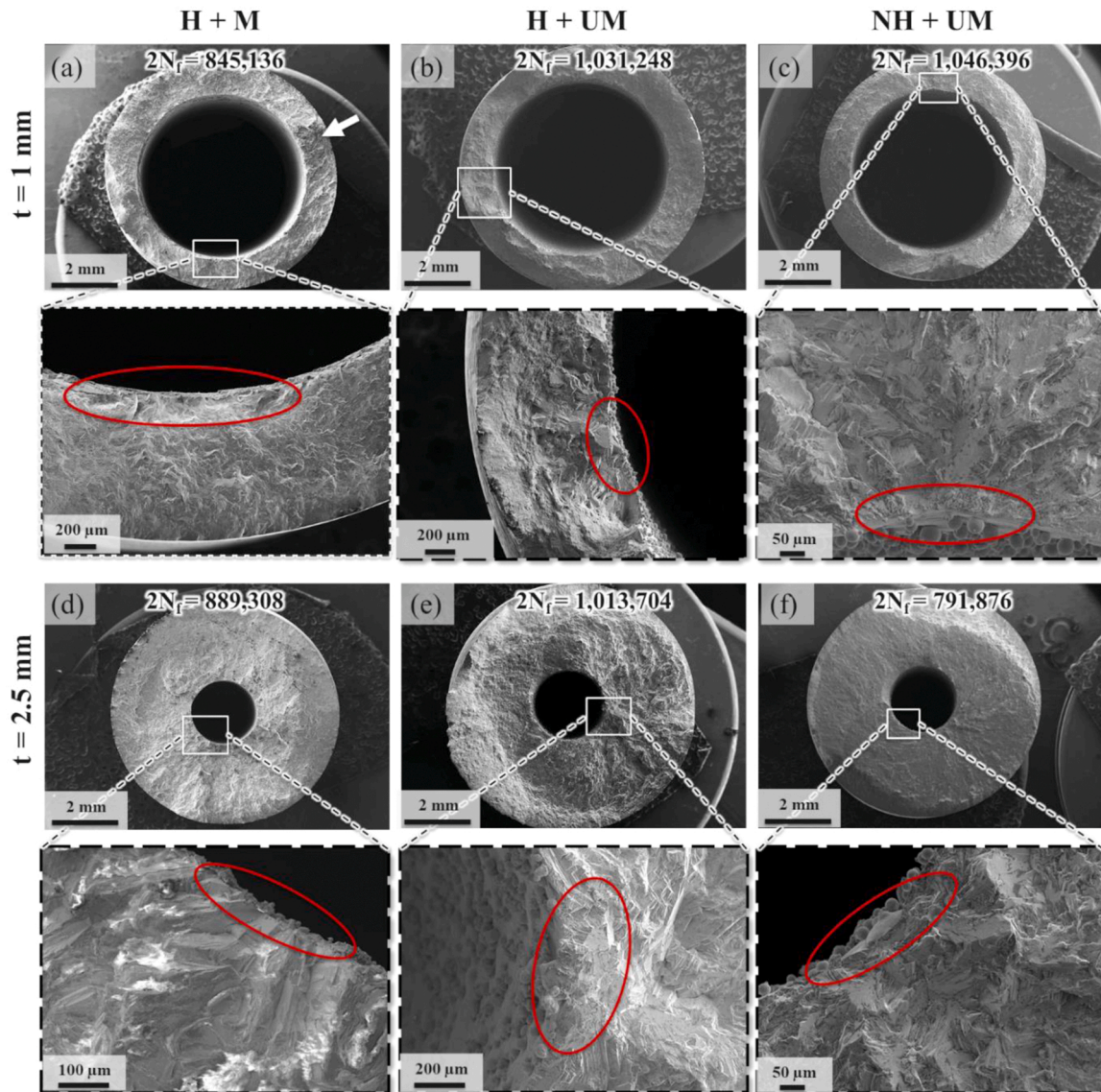
**Fig. 15.** Fatigue fracture surfaces of NFC specimens with different thicknesses and post-processing conditions tested at $\varepsilon_a = 0.002$ mm/mm: (a) t = 1 mm H + M, (b) t = 1 mm H + UM, (c) t = 1 mm NH + UM, (d) t = 2.5 mm H + M, (e) t = 2.5 mm H + UM, and (f) t = 2.5 mm NH + UM. White arrow points at crystallographic facets, while red ellipses indicate surface notches.

## 5. Conclusions

The objective of this study was to investigate the effects of hot isostatic pressing (HIP), machining, and specimen wall thickness on the tensile and fatigue behaviors of L-PBF thin wall and narrow flow channel IN718 parts. Based on the results, the following conclusions can be drawn:

1. NonHIP specimens had slightly higher yield strength (by ~100 MPa or ~10%) compared to HIP ones. This was attributed to the finer grain size and dendritic microstructure of NonHIP specimens.
2. HIP specimens showed better elongation to failure (by ~20%) compared to NonHIP ones. This was due to carbide debonding governing the fracture mechanism in HIP specimens, unlike NonHIP ones where excessive precipitation of brittle $\delta$ phases provided abundant sites for void nucleation and coalescence which resulted in an earlier fracture.
3. Higher elongation to failure was observed for thicker HIP and machined specimens (by ~20%) due to the proportional relation between toughness and thickness in the plane stress fracture mode.

The fracture mode of HIP and unmachined specimens was plane strain, and therefore, did not show such a trend.

4. Under cyclic loading, multiples cracks initiated from both internal and external surfaces of specimens at early stages, regardless of post-processing and thickness. Crack propagation occupied a major portion of fatigue life in low to mid cycle fatigue regimes.
5. The fatigue crack initiation in thin wall specimens under the HIP and machined condition was governed by persistent slip bands (PSBs), which were easier to form/operate in thinner walls. Therefore, longer fatigue lives with an increase in thickness in high cycle fatigue regime (by a factor ~2) was observed. On the other hand, only surface governed fatigue crack initiation was observed in the narrow flow channel specimens, as a result, they did not exhibit dependence on thickness.
6. NonHIP and unmachined thin wall specimens with thickness of 0.50 mm showed higher fatigue lives in high cycle fatigue regime (by a factor of ~2) compared the ones with identical thickness under HIP condition. This was ascribed to more grains through wall thickness of NonHIP specimens and presence of abundant $\delta$ phase, which resisted earlier crack initiations from PSBs and led to a better fatigue

resistance. The effect of machining on fatigue behavior was not significant in these specimens.

7. Overall, the effect of HIP and/or machining on low to mid cycle fatigue regimes was insignificant. Although HIP slightly improved fatigue lives of thin wall specimens with t = 1.25 mm in high cycle fatigue regime, it did not influence the fatigue behavior of narrow flow channel geometries. In either geometry, machining did not improve the fatigue resistance of HIP specimens.

Post-processing operations (i.e., HIP and/or surface machining) are costly, time-consuming, and challenging in thin wall and narrow flow channel geometries. This study demonstrated that HIP and machining operation were not beneficial for IN718 in low to mid cycle fatigue regimes and to some extent neither in high cycle fatigue regime. Therefore, the lead time and cost for additive manufacturing of these geometries can be substantially reduced for IN718 by eliminating HIP and machining steps form production process without significant debits in mechanical performance.

## CRediT authorship contribution statement

**Nabeel Ahmad:** Visualization, Validation, Methodology, Investigation, Formal analysis, Data curation, Conceptualization, Writing - original draft, Writing - review & editing. **Shuai Shao:** Resources, Methodology, Investigation, Formal analysis, Conceptualization, Writing - review & editing. **Mohsen Seifi:** Methodology, Conceptualization, Writing - review & editing. **Nima Shamsaei:** Supervision, Resources, Project administration, Methodology, Investigation, Formal analysis, Conceptualization, Funding acquisition, Writing - review & editing.

## Declaration of Competing Interest

The authors declare that they have no known competing financial interests or personal relationships that could have appeared to influence the work reported in this paper.

## Data Availability

Data will be made available on request.

## Acknowledgement

## References

[1] G. Wu, G. Li, W. Pan, I. Raja, X. Wang, S. Ding, A state-of-art review on chatter and geometric errors in thin-wall machining processes, J. Manuf. Process 68 (2021) 454–480, https://doi.org/10.1016/j.jmapro.2021.05.055.

[2] S. Roy, R. Kumar, Anurag, A. Panda, R.K. Das, A brief review on machining of inconel 718, Mater. Today Proc. 5 (2018) 18664–18673, https://doi.org/10.1016/j.matpr.2018.06.212.

[3] D. Keiser, H.L. Brown, A Rev. Phys. Metall. ALLOY 718 (1976), https://doi.org/10.2172/4016087.

[4] N. Shamsaei, A. Yadollahi, L. Bian, S.M. Thompson, An overview of Direct Laser Deposition for additive manufacturing; part II: mechanical behavior, process parameter optimization and control, Addit. Manuf. 8 (2015) 12–35, https://doi.org/10.1016/j.addma.2015.07.002.

[5] R. Russell, D. Wells, J. Waller, B. Poorganji, E. Ott, T. Nakagawa, et al., Qualification and certification of metal additive manufactured hardware for aerospace applications, Elsevier Inc, 2019, https://doi.org/10.1016/B978-0-12-814062-8.00003-0.

[6] T. DebRoy, H.L. Wei, J.S. Zuback, T. Mukherjee, J.W. Elmer, J.O. Milewski, et al., Additive manufacturing of metallic components – process, structure and properties, Prog. Mater. Sci. 92 (2018) 112–224, https://doi.org/10.1016/j.pmatsci.2017.10.001.

[7] J. Pegues, M. Roach, R. Scott Williamson, N. Shamsaei, Surface roughness effects on the fatigue strength of additively manufactured Ti-6Al-4V, Int. J. Fatigue 116 (2018) 543–552, https://doi.org/10.1016/j.ijfatigue.2018.07.013.

[8] J.W. Pegues, N. Shamsaei, M.D. Roach, R.S. Williamson, Fatigue life estimation of additive manufactured parts in the as-built surface condition, Mater. Des. Process Commun. 1 (2019), e36, https://doi.org/10.1002/mdp2.36.

[9] D.T. Ardi, L. Guowei, N. Maharjan, B. Mutiargo, S.H. Leng, R. Srinivasan, Effects of post-processing route on fatigue performance of laser powder bed fusion Inconel 718, Addit. Manuf. 36 (2020) 101442, https://doi.org/10.1016/j.addma.2020.101442.

[10] S. Gribbin, S. Ghorbanpour, N.C. Ferreri, J. Bicknell, I. Tsukrov, M. Knezevic, Role of grain structure, grain boundaries, crystallographic texture, precipitates, and porosity on fatigue behavior of Inconel 718 at room and elevated temperatures, Mater. Charact. 149 (2019) 184–197, https://doi.org/10.1016/j.matchar.2019.01.028.

[11] M.E. Aydinöz, F. Brenne, M. Schaper, C. Schaak, W. Tillmann, J. Nellesen, et al., On the microstructural and mechanical properties of post-treated additively manufactured Inconel 718 superalloy under quasi-static and cyclic loading, Mater. Sci. Eng. A 669 (2016) 246–258, https://doi.org/10.1016/j.msea.2016.05.089.

[12] A.R. Balachandramurthi, J. Moverare, N. Dixit, R. Pederson, Influence of defects and as-built surface roughness on fatigue properties of additively manufactured Alloy 718, Mater. Sci. Eng. A 735 (2018) 463–474, https://doi.org/10.1016/j.msea.2018.08.072.

[13] E. Sadeghi, P. Karimi, N. Israelsson, J. Shipley, T. Månsson, T. Hansson, Inclusion-induced fatigue crack initiation in powder bed fusion of Alloy 718, Addit. Manuf. 36 (2020), 101670, https://doi.org/10.1016/j.addma.2020.101670.

[14] S. Gribbin, S. Ghorbanpour, N.C. Ferreri, J. Bicknell, I. Tsukrov, M. Knezevic, Role of grain structure, grain boundaries, crystallographic texture, precipitates, and porosity on fatigue behavior of Inconel 718 at room and elevated temperatures, Mater. Charact. 149 (2019) 184–197, https://doi.org/10.1016/j.matchar.2019.01.028.

[15] S. Gribbin, J. Bicknell, L. Jorgensen, I. Tsukrov, M. Knezevic, Low cycle fatigue behavior of direct metal laser sintered Inconel alloy 718, Int J. Fatigue 93 (2016) 156–167, https://doi.org/10.1016/j.ijfatigue.2016.08.019.

[16] M. Muhammad, P. Frye, J. Simsiriwong, S. Shao, N. Shamsaei, An investigation into the effects of cyclic strain rate on the high cycle and very high cycle fatigue behaviors of wrought and additively manufactured Inconel 718, Int J. Fatigue 144 (2021), 106038, https://doi.org/10.1016/j.ijfatigue.2020.106038.

[17] M.S. Dodaran, M. Muhammad, N. Shamsaei, S. Shao, Synergistic effect of microstructure and defects on the initiation of fatigue cracks in additively manufactured inconel 718, Int J. Fatigue (2022), 107002, https://doi.org/10.1016/j.ijfatigue.2022.107002.

[18] X. Zhao, A. Rashid, A. Strondl, C. Hulme-Smith, N. Stenberg, S. Dadbakhsh, Role of superficial defects and machining depth in tensile properties of electron beam melting (EBM) made inconel 718, J. Mater. Eng. Perform. 30 (2021) 2091–2101, https://doi.org/10.1007/s11665-021-05487-9.

[19] S. Götelid, T. Ma, C. Lyphout, J. Vang, E. Stålnacke, J. Holmberg, et al., Effect of post-processing on microstructure and mechanical properties of Alloy 718 fabricated using powder bed fusion additive manufacturing processes, Rapid Prototyp. J. 27 (2021) 1617–1632, https://doi.org/10.1108/RPJ-12-2019-0310.

[20] W. Everhart, E. Sawyer, T. Neidt, J. Dinardo, B. Brown, The effect of surface finish on tensile behavior of additively manufactured tensile bars, J. Mater. Sci. 51 (2016) 3836–3845, https://doi.org/10.1007/s10853-015-9702-9.

[21] S. Lee, S. Shao, D.N. Wells, M. Zetek, M. Kepka, N. Shamsaei, Fatigue behavior and modeling of additively manufactured IN718: The effect of surface treatments and surface measurement techniques, J. Mater. Process Technol. 302 (2022), 117475, https://doi.org/10.1016/j.jmatprotec.2021.117475.

[22] A. Yadollahi, N. Shamsaei, Additive manufacturing of fatigue resistant materials: Challenges and opportunities, Int J. Fatigue 98 (2017) 14–31, https://doi.org/10.1016/j.ijfatigue.2017.01.001.

[23] America Makes, AMSC. Standardization Roadmap for Additive Manufacturing - Version 2.0. vol. 2. 2018.

[24] J. Schneider, Comparison of microstructural response to heat treatment of inconel 718 prepared by three different metal additive manufacturing processes, JOM 72 (2020) 1085–1091, https://doi.org/10.1007/s11837-020-04021-x.

[25] A. Soltani-Tehrani, R. Shrestha, N. Phan, M. Seifi, N. Shamsaei, Establishing specimen property to part performance relationships for laser beam powder bed fusion additive manufacturing, Int. J. Fatigue 151 (2021), 106384, https://doi.org/10.1016/j.ijfatigue.2021.106384.

[26] M. Seifi, M. Gorelik, J. Waller, N. Hrabe, N. Shamsaei, S. Daniewicz, et al., Progress towards metal additive manufacturing standardization to support qualification and certification, JOM 69 (2017) 439–455, https://doi.org/10.1007/s11837-017-2265-2.

[27] S.M.J. Razavi, B. Van Hooreweder, F. Berto, Effect of build thickness and geometry on quasi-static and fatigue behavior of Ti-6Al-4V produced by Electron Beam Melting, Addit. Manuf. 6 (2020), 101426, https://doi.org/10.1016/j.addma.2020.101426.

[28] C.H. Yu, A. Leicht, R.L. Peng, J. Moverare, Low cycle fatigue of additively manufactured thin-walled stainless steel 316L, Mater. Sci. Eng. A 821 (2021), 141598, https://doi.org/10.1016/j.msea.2021.141598.

[29] T. Modulus C. Modulus H. Rates S. Rates C. Axial F. Standard Practice for Strain-Controlled Axial-Torsional Fatigue Testing with Thin-. Annu B ASTM Stand 2010;i: 1–8. https://www.astm.org/e2207-15r21.html.

[30] Standard for Additive Manufacturing – Post Processing Methods – Standard Specification for Thermal Post-Processing Metal Parts Made Via Powder Bed Fusion 2018 ASTM Stand. https://www.astm.org/f3301-18a.html.

[31] Heat Treatment Nickel Alloy and Cobalt Alloy Parts. 2020. https://www.sae.org/standards/content/ams2774/.

[32] Interanational AE– 11 (Reapproved 2017). Standard Guide for Preparation of Metallographic Specimens Standard Guide for Preparation of Metallographic Specimens 1. vol. 03.01. 2012. https://www.astm.org/e0003-11r17.html.

[33] AE. Committee E08 Standard Test Methods for Tension Testing of Metallic Materials ASTM International; 2020. https://www.astm.org/e0008_e0008m-22.html.

[34] E606 A. Standard Test Method for. ASTM International;2020. https://doi.org/10.1520/mnl10913m.

[35] S. Azadian, L.-Y. Wei, R. Warren, Delta phase precipitation in Inconel 718, Mater. Charact. 53 (2004) 7–16, https://doi.org/10.1016/j.matchar.2004.07.004.

[36] L. Liu, Q. Ding, Y. Zhong, J. Zou, J. Wu, Y.L. Chiu, et al., Dislocation network in additive manufactured steel breaks strength–ductility trade-off, Mater. Today 21 (2018) 354–361, https://doi.org/10.1016/j.mattod.2017.11.004.

[37] T.G. Gallmeyer, S. Moorthy, B.B. Kappes, M.J. Mills, B. Amin-Ahmadi, A. P. Stebner, Knowledge of process-structure-property relationships to engineer better heat treatments for laser powder bed fusion additive manufactured Inconel 718, Addit. Manuf. 31 (2020), 100977, https://doi.org/10.1016/j.addma.2019.100977.

[38] M.A. Meyers, K.K. Chawla. Mechanical Behavior of Materials, second ed., Cambridge University Press, Cambridge, 2009.

[39] Y.L. Kuo, S. Horikawa, K. Kakehi, The effect of interdendritic δ phase on the mechanical properties of Alloy 718 built up by additive manufacturing, Mater. Des. 116 (2017) 411–418, https://doi.org/10.1016/j.matdes.2016.12.026.

[40] N. Ahmad, R. Ghiaasiaan, P.R. Gradl, S. Shao, N. Shamsaei, Revealing deformation mechanisms in additively manufactured Alloy 718: cryogenic to elevated temperatures, Mater. Sci. Eng. A 849 (2022), 143528, https://doi.org/10.1016/j.msea.2022.143528.

[41] R.I. Stephens, A. Fatemi, R.R. Stephens, H.O. Fuchs. Metal Fatigue in Engineering, second ed., John Wiley & Sons, 2000.

[42] E. Vanswijgenhoven, J. Holmes, Fatigue crack growth in inconel 718 superalloy foil at elevated temperature, Proc. Int Symp. Superalloys Var. Deriv. 1 (2001) 669–678, https://doi.org/10.7449/2001/superalloys_2001_669_678.

[43] L.A. James, W.J. Mills, Effect of heat-treatment and heat-to-heat variations in the fatigue-crack growth response of alloy 718, Eng. Fract. Mech. 22 (1985) 797–817, https://doi.org/10.1016/0013-7944(85)90109-2.

[44] Y.N. Hu, S.C. Wu, P.J. Withers, J. Zhang, H.Y.X. Bao, Y.N. Fu, et al., The effect of manufacturing defects on the fatigue life of selective laser melted Ti-6Al-4V structures, Mater. Des. (2020) 192, https://doi.org/10.1016/j.matdes.2020.108708.

[45] S. Romano, A. Brandão, J. Gumpinger, M. Gschweitl, S. Beretta, Qualification of AM parts: extreme value statistics applied to tomographic measurements, Mater. Des. 131 (2017) 32–48, https://doi.org/10.1016/j.matdes.2017.05.091.

[46] S.C. Wu, T.Q. Xiao, P.J. Withers, The imaging of failure in structural materials by synchrotron radiation X-ray microtomography, Eng. Fract. Mech. 182 (2017) 127–156, https://doi.org/10.1016/j.engfracmech.2017.07.027.

[47] N. Shamsaei, A. Fatemi, Small fatigue crack growth under multiaxial stresses, Int J. Fatigue 58 (2014) 126–135, https://doi.org/10.1016/j.ijfatigue.2013.02.002.

[48] James L.A. The Effect of Product Form Upon Fatigue-Crack Growth Behavior of Alloy 718 1981;103.

[49] S. Gribbin, S. Ghorbanpour, N.C. Ferreri, J. Bicknell, I. Tsukrov, M. Knezevic, Role of grain structure, grain boundaries, crystallographic texture, precipitates, and porosity on fatigue behavior of Inconel 718 at room and elevated temperatures, Mater. Charact. 149 (2019) 184–197, https://doi.org/10.1016/j.matchar.2019.01.028.

[50] M.D. Sangid, The physics of fatigue crack initiation, Int. J. Fatigue 57 (2013) 58–72, https://doi.org/10.1016/j.ijfatigue.2012.10.009.